Sensory responses of visual cortical neurons are not prediction errors

Jacob A. Westerberg[1,2,†], Yihan S. Xiong[1,†], Eli Sennesh[1], Hamed Nejat[1], David Ricci[1], Séverine Durand[3], Ben Hardcastle[3], Hannah Cabasco[3], Hannah Belski[3], Ahad Bawany[3], Ryan Gillis[3], Henry Loeffler[3], Carter R. Peene[3], Warren Han[3], Katrina Nguyen[3], Vivian Ha[3], Tye Johnson[3], Conor Grasso[3], Ahrial Young[3], Jackie Swapp[3], Ben Ouellette[3], Shiella Caldejon[3], Ali Williford[3], Peter A. Groblewski[3], Shawn R. Olsen[3], Carly Kiselycznyk[3], Christof Koch[3], Jerome A. Lecoq[3], Alexander Maier[1], and André M. Bastos[1,*]

[1]Department of Psychology, Vanderbilt Brain Institute, Vanderbilt Vision Research Center, Vanderbilt University, Nashville, United States

[2]Department of Vision and Cognition, Netherlands Institute for Neuroscience, Royal Netherlands Academy of Arts and Sciences, Amsterdam, The Netherlands

[3]Allen Institute for Brain Science, Seattle, United States.

[*]Corresponding author. Email: andre.bastos@vanderbilt.edu

[†]These authors contributed equally to this work

Abstract

Predictive coding is theorized to be a ubiquitous cortical process to explain sensory responses. It asserts that the brain continuously predicts sensory information and imposes those predictions on low-level sensory areas to shape perception and guide behavior. We tested predictive coding using a visual oddball task in mice and monkeys. By combining neurophysiology and optogenetics in multiple visual cortical areas, we refute predictive coding as a ubiquitous computation throughout neocortex. Highly predictable stimuli were never explained away, and highly unpredictable oddballs did not evoke omnipresent prediction errors. Visual sensory cortex robustly signaled highly predictable information and was dampened by repetition-based adaptation. Prediction-based modulations were restricted to higher-order cortex. Therefore, visual sensory processing is dominated by feedforward activation, with predictions modulating sensory responses, not defining them.

Main Text

Predictions shape our perception, and it is often immediately apparent when predictions are violated (*1*). Predictive coding (PC) has emerged as a leading theoretical framework to explain how predictions are instantiated in the brain (*2*, *3*). One likely reason for the appeal of PC is its broad explanatory power despite its simplicity: a few theoretical constructs (prior probabilities/predictions, incoming data, prediction errors) account for a large host of neurophysiological and psychological phenomena. These phenomena range from mismatch negativity (*4*), sensory processing (*5*), and adaptation (*6*) to attentional modulation (*7–9*). It has even been proposed that PC models can be a building block to understand conscious experience (*10*).

Predictive coding (PC) models make a series of testable hypotheses (schematized in Fig. 1) about the mechanisms of neuronal processing (*3*, *11–14*). Specifically, PC proposes that the brain compares incoming sensory information against a prediction signal. Predictions are transmitted to sensory areas, and if an incoming sensory signal matches the prediction, the two signals cancel. Thus, predicted sensory data are "explained away," resulting in reduced neural activity. Prior studies in monkeys and mice have yielded mixed results on the nature and extent of prediction error coding in mammalian sensory cortex (*5*, *15–19*). The apparent discrepancies between studies could be due to differences in paradigm, species, and areas studied. A core controversy has been whether prediction "errors" mostly reflect a release from cortical adaptation to repeated inputs vs. a more complex predictive computation (*15*, *18*, *20*). Consequently, the fundamental questions of whether and how predictive coding emerges across the cortical hierarchy and whether it is a shared mammalian cortical computation remain unanswered.

To resolve this, we tested PC using Multi-Area, high-Density, Laminar-resolved Neurophysiology (MaDeLaNe) recordings of thousands of spiking neurons in mice and monkeys throughout the visual cortex (areas V1, LM, RL, AL, PM, AM in mice and areas V1, V2, V3, V4, MT, MST in monkeys) and prefrontal cortex (areas 8A and the lateral PFC in monkeys). We used a variation of the global-local oddball task, which disentangles short-term stimulus repetition (causing neuronal adaptation) from prediction (*21*). Mice and monkeys were habituated to a "local oddball" sequence (x-x-x-y) for thousands of trials across several days before recording neuronal responses to surprising "global oddball" sequences (x-x-x-x) to test for neuronal signaling of prediction errors.

We tested three core PC hypotheses (*2*, *3*, *11*, *12*) regarding prediction error signaling in spike rates (Fig. 1A). The first hypothesis (H1) is that predictions are subtractive. If so, they should (a) diminish the response to highly predictable stimuli (local oddballs), and (b) they should activate specific inhibitory interneuron cell populations and there should be a release from their inhibition during prediction errors. The second hypothesis

(H2) is that prediction errors are fed forward. If so, then unpredicted, i.e., novel stimuli should evoke prediction errors that (a) are triggered early in the sensory response (within the first 50-150 ms of processing that constitute the feedforward sweep (*22*, *23*)), (b) emerge early in the visual sensory cortical hierarchy and then, with progressive delays in higher areas, (c) evoke activity in pyramidal neurons in superficial layers (L2/3) of the cortex, as feedforward projections predominantly project from these neurons (*24*), and (d) evoke feedforward directed functional connectivity between neurons. The third hypothesis (H3) is that prediction error signaling is a canonical neocortical computation (*11*). If so, global oddball signaling should be robust and widespread across different cortical areas and species.

Results

We first extensively habituated animals to the local oddball x-x-x-y stimulus sequence for 2000-3000 trials over several days (Fig. 1B and Fig. S1). The "x" and "y" stimuli within a sequence denote drifting gratings at 135 or 45 degrees from horizontal and were counterbalanced across sessions/animals. The unpredictable global oddball x-x-x-x stimulus sequence was never presented during habituation and introduced only on neural recording sessions (Fig. 1C), on 20% of trials in the main block (Fig. 1B). This long habituation period ensured that animals could learn to predict the x-x-x-y (local oddball) stimulus sequence. Indeed, pupillary responses suggested that animals recognized the violation of this sequence during unpredicted x-x-x-x global oddballs (Fig. S2).

To investigate the neuronal signaling underlying these predictions, we compared responses in the main block to a control block where the x-x-x-x sequence alternated with y-y-y-y and thus the sequence was predictable after the first stimulus (Fig. 1B). To analyze global and local oddballs, we compared spiking responses to the 4th component in the sequence (P4) to the same stimulus in the same sequence position of the control block (vertical dotted lines in Fig. 1B). To account for cross-session firing rate drift which occurs even in well-isolated single units (*25*), we normalized responses to the third component in the sequence (P3). Our main contrast was therefore P4-P3 in the main block vs. P4-P3 in the control block. For global oddballs, this contrast should reveal prediction errors while controlling for short-term adaptation. For local oddballs, this contrast should reveal the release of adaptation caused by changing the stimulus after a few repetitions. Neurons responded to these sequences with robust firing rate increases in all recorded areas (Fig. 1D, S7, S8). Significant oddball detection was determined by comparing the neuronal spiking response for each oddball type using a nonparametric, cluster-based permutation test (*26*) (at $P < 0.05$, corrected for multiple comparisons, see *Materials and Methods*).

Highly predictable local oddballs are signaled with a robust, widespread response

Because of extensive habituation, local oddballs were non-surprising stimuli and, according to PC, should be suppressed and explained away (H1a). However, we observed that neuronal signaling of local oddballs was ubiquitous (present in all areas and both species, Fig. 2A), signaled early and fed forward up the visual cortical hierarchy (within the first ~150 ms of stimulus processing, Fig. 2B), strong (local oddball responses by area were on average 60-98% above the control stimulus in mice, and 43%-93% in monkeys, Fig. 2C), and involved more than 50% of all recorded neurons (median across areas in mice: 51%, median across areas in monkeys: 65%, Fig 2D). In mice but not monkeys, local oddball signaling gradually increased in strength with ascending cortical hierarchy (Linear correlation between local oddball response and hierarchical area, $R^2 = 0.83$, P=5.75e-5, Fig. 2C, left subpanel). In monkeys, the local oddball response was strongest in area MT (ANOVA, $p<0.001$, Fig. 2C, right subpanel). In V1 of both species, local oddball signaling was most prominent amongst neurons in L2/3 neurons (Fig. 2E; for details on layer identification, see *Materials and Methods* and Fig. S5).

Can these local oddball responses, representing local signal change, could be considered a simple form of prediction error signaling? To examine this, we compared the local oddballs in contexts that differed in their relative probability (local oddball sequence probability varied between 100%, 80%, and 12.5%, see Fig. S1). If they represent prediction errors, local oddball responses should scale according to their deviance (H1a). We found that local oddball signaling did not scale as a function of deviance in most areas (Fig. S9, area V4 was an exception). Instead, we observed the opposite pattern just as often, and most prominently in V1 of mice (Fig. S9B). The enhanced neuronal responses to more predictable local oddballs in mouse V1 may have been caused by learning-driven potentiation (*27*). To summarize, local oddball sequences (x-x-x-y) release most neurons from adaptation and increase excitability independent of prediction, even though animals had been exposed to these sequences thousands of times.

Highly unpredictable global oddballs are not signaled with feedforward prediction error

Next, we tested whether highly surprising global oddballs (x-x-x-x) drive neuronal spiking consistent with prediction error signaling. We found that global oddball signaling was restricted to only a few higher-order brain areas (LM, AM, and PM in mice; V3, MT, 8A, and PFC in monkeys, Fig. 3A). At the individual neuron level, although we identified a handful of neurons/areas that responded to global oddballs (Fig. S7 & S8), the percentage of units signaling global oddballs in each area was sparse (median across areas in mice: 7%, median across areas in monkeys: 8%, Fig. 3B), contradicting H3. Unlike local oddballs, which showed a clear temporal

progression of latencies across the hierarchy (Fig. 2C), the latency at which neurons signaled global oddballs did not scale with hierarchy (Fig. 3C).

We next examined global oddballs within L2/3 pyramidal neurons, which according to PC should transmit prediction error (H2). In mice, we found that putative layer 2/3 pyramidal cells did not signal global oddballs (Fig. S6A). In addition, current source density analysis (see *Materials and Methods*) of synaptic activity in L2/3 of mice did not reveal any reliable changes in synaptic activation (Fig. S4A,B) during global oddballs. In monkeys, L2/3 spiking activity did not signal global oddballs in area V3 (Fig. S6B). There was L2/3 involvement in global oddballs in area MT, but this came 116 ms later than in area PFC, supporting a feedback (*22*, *28*) rather than feedforward putative error computation (Fig. S6B).

Without the hypothesized L2/3-specific signal, we investigated alternative sources for global oddball signaling. We limited the analysis to the areas with population global oddball signaling. We grouped areas into higher- and lower-order (higher-order areas AM and PM vs. lower-order area LM in mice; higher-order area PFC vs. lower-order areas V3 and MT in monkeys). We first divided the units into granular (L4) vs. extragranular (L2/3 and L5/6) compartments, which anatomically separate feedforward vs. feedback inputs (*28*). In mice, we observed global oddball signalling only in the extragranular (feedback-associated) layers and later in the lower-order cortex (401 ms post-stimulus, Fig. 3B, left sub-panels) than in the higher-order cortex (337 ms post-stimulus). In monkey visual areas V3 and MT, we observed global oddball signaling only in the extragranular (feedback-associated) layers (135 ms post-stimulus), later in time than the extragranular layers of higher-order area PFC (111 ms post-stimulus, Fig. 3B, right sub-panels). These latency and laminar effects collectively support prediction error propagation from higher to lower areas of the hierarchy, contradicting H2.

Finally, we also analyzed whether global oddballs were more consistently signaled in the first few trials when they occurred early in the main block, when putative prediction errors should be strongest. Although area V4 in monkeys and PM in mice exhibited a profile consistent with a putative prediction error signal, areas before or after them in the hierarchy did not (Fig. S11), inconsistent with the hypothesized feedforward (H2) or with an ubiquitous (H3) prediction error signal.

Directed connectivity of global oddballs does not indicate feedforward error propagation

In PC, prediction errors are sent feedforward (Fig. 1A, H2). Hence, neurons earlier in the hierarchy should increase their drive onto neurons later in the hierarchy to signal prediction error. We tested this by computing Granger causality between spiking activity time courses. Granger causality tests whether neuronal activity in

area A can statistically predict activity in area B above and beyond predictions made by activity in area B alone (*29*). If so, then area A "Granger-causes" B. By comparing the A-to-B vs. the B-to-A directions of Granger causality (*30*) where A is below B in the hierarchy, we tested whether local and global oddballs evoked feedforward processing. In mice, compared to pre-stimulus baseline (Fig. S3A), the hierarchy became more feedforward-dominated in both early (100-300 ms) and late (300-500 ms) periods of local oddball processing (Fig. S3A and B, Wilcoxon ranksum test, $P<0.01$). This feedforward activity propagated from V1 to the highest levels of the visual hierarchy, area PM. In contrast, during global oddballs, there was no change in feedforward vs. feedback asymmetry compared to baseline (Fig. S3B-D, Wilcoxon rank sum test of GC asymmetry values across mice vs. pre-oddball baseline, all comparisons, $P>0.01$). To summarize, the latency, hierarchical areas of significant signaling, laminar, and Granger analyses collectively contradicted H2; namely, global oddballs did not drive feedforward processing. Instead, the data supported a feedback model for processing prediction errors evoked by global oddballs.

Global oddballs: A release from predictive inhibition?

In PC, predictions are hypothesized to subtract away predictable stimuli (H1b), leaving sensory cortex less excited. We tested this by assessing whether predictions are neuronally instantiated by inhibitory interneuron activity. We used optogenetics to identify Somatostatin- (SST) and Parvalbumin- (PV) expressing interneurons in mice, and a viral vector tool that restricted optogenetic expression to inhibitory interneurons in monkeys (*31*) (Fig. 4A and Fig. S10). In both species, we utilized Channelrhodopsin-2 to drive the inhibitory interneurons to fire during light stimulation (using a sinusoidal light stimulation protocol; see *Materials and Methods*). In mice, PV+/SST+ units were identified across all recorded areas and in monkeys, inhibitory interneurons were identified in areas MT/MST, PFC, and 8A (Fig. 4B). In monkeys, opto-tagged neurons had on average narrow waveform characteristics, additional confirmatory evidence (*32*) that these opto-tagged neurons were inhibitory (Fig. 4B). In both species, these inhibitory cell populations responded to the stimulus sequence and increased their spike rates during P4 of local oddballs (Fig. 4C). However, we did not observe a significant response to global oddballs at the population average of these subpopulations (Fig. 4D; for P3 and P4 components see Fig. S7B). This indicates a minor role, if any, for these inhibitory interneuron sub-populations in signaling global oddballs, failing to support H1b.

Discussion

To test the neuronal implementation of PC, we performed an extensive survey of cortical spiking in mice and monkeys observing predictable or unpredictable stimulus sequences. We used MaDeLaNe (Multi-Area, high-

Density, Laminar Neurophysiology) recordings (*20*) and optogenetics to isolate different cortical layers, areas, and neuron types previously hypothesized to play a role in PC (*2*, *3*, *12*, *33*). We tested whether neuronal spiking responses could be described as prediction error signals resulting from a release from predictive suppression (H1), and that triggers feedforward processing (H2) with a robust and ubiquitous signature (H3).

PC models have hypothesized that prediction errors constitute a core, feedforward cortical computation (*2*, *3*, *12*, *33*). Our subjects were habituated to a particular sequence (x-x-x-y) for thousands of trials such that its violation (x-x-x-x) should drive robust spike signaling of prediction error. In PC, the habituated (and highly predictable) local oddballs (x-x-x-y) should be explained away, driving minimal activity (*34*). We found the exact opposite: spiking responses robustly signaled unsurprising local oddballs (engaging over 50% of all recorded neurons) but weakly signaled surprising global oddballs (engaging less than 10% of all recorded neurons). Local oddballs emerged early in the hierarchy at fast latencies in layers 2/3, and fed forward up the cortical hierarchy (Fig. 5A). However, contradicting the interpretation of these signals as prediction errors, local oddball responses did not consistently scale with increased sequence deviance, and did not trigger a release of inhibition from inhibitory interneurons (contradicting H1). Therefore, local oddball processing is most likely explained as a release from neuronal adaptation.

PC models hypothesized that L2/3 pyramidal neurons transmit feedforward prediction errors. Global oddballs, which should have triggered this hypothesized feedforward flow, emerged late in the sensory response and in higher-order areas first, then lower-order regions (Fig. 5B). Putative excitatory pyramidal neurons in L2/3 (which project feedforward connections) and their associated current sinks did not signal global oddballs in mice and only signaled weakly in one area (monkey area MT) and later than in PFC. Instead, global oddballs were found to emerge at the population level in the non-granular, feedback-recipient layers. Feedforward enhancement of functional connectivity assessed by Granger causality was not observed during global oddballs. Therefore, we failed to detect feedforward processing during global oddballs by four independent metrics: hierarchical area, temporal order, Granger causality, and laminar compartment of spiking/transmembrane current flow (Fig. 5B, contradicting H2). Further, global oddballs did not emerge as a result of a release of inhibition from PV/SST+ interneurons in mice or the population of inhibitory interneurons in monkeys (contradicting H1). Our results speak against the proposed ubiquity of prediction error signaling in sensory cortex (contradicting H3).

Our results challenge current PC models (*3*, *12*, *12*, *33*). Rather than a ubiquitous property, predictive coding is largely a property of neurons in higher-order cortex (PFC in primates, and late stages of visual processing in

both species). These higher-order areas, which have evidence for PC (*16*, *20*, *35*), engage visual areas with weak, modulatory feedback signals that do not drive a subtractive feedforward prediction error computation in visual cortex (as PC hypothesized). These observations are congruent with the fact that neurons in the visual sensory cortex have receptive field properties defined by the long time-scales of brain development (*36*) and are therefore ill-suited for predictive computations that change at fast behavioral time scales. Neurons in higher-order areas are more flexible in their response preferences. These higher-order neurons can re-map their activity in real-time based on experience-dependent learning, and display mixed-selectivity (*37*). This property is necessary for predictive coding because predictions need to be sensitive to the statistical structure of a changing and context-dependent environment (*35*, *38*). We hypothesize that mixed selectivity neurons flexibly remap cognitive spaces (*39*) to signal predictions. Functionally, such neurons could form dynamic ensembles via neuronal oscillations (*20*, *40–42*) to guide sensory processing.

To summarize, rather than signaling prediction errors, we found that a more powerful driver of spiking activity in the visual sensory cortex is stimulus feature and (release from) short-term adaptation. Rather than a canonical computation, the detection of surprising sequences is an emergent feature of higher-order cortex. We speculate that this neuronal architecture may reflect a trade-off between accuracy (via faithful preservation of stimulus information in sensory cortex) and efficiency (via predictive coding in higher-order cortex). In addition, a sensory system more driven by stimulus information than internal predictive information is less likely to confuse top-down inputs with sensory inputs, and therefore more robust to hallucinations and delusions (*43*). Simultaneously, predictive coding can be implemented at higher levels of the hierarchy, to efficiently encode, filter and select relevant sensory signals.

References and Notes

1. L. Itti, P. Baldi, Bayesian surprise attracts human attention. *Vision Res.* **49**, 1295–1306 (2009).
2. K. Friston, The free-energy principle: a unified brain theory? *Nat. Rev. Neurosci.* **11**, 127–138 (2010).
3. R. P. N. Rao, D. H. Ballard, Predictive coding in the visual cortex: a functional interpretation of some extra-classical receptive-field effects. *Nat. Neurosci.* **2**, 79–87 (1999).
4. M. I. Garrido, J. M. Kilner, S. J. Kiebel, K. J. Friston, Evoked brain responses are generated by feedback loops. *Proc. Natl. Acad. Sci. U. S. A.* **104**, 20961–20966 (2007).
5. C. M. Schwiedrzik, W. A. Freiwald, High-Level Prediction Signals in a Low-Level Area of the Macaque Face-Processing Hierarchy. *Neuron* **96**, 89-97.e4 (2017).
6. T. Hosoya, S. A. Baccus, M. Meister, Dynamic predictive coding by the retina. *Nature* **436**, 71–77 (2005).
7. H. R. Brown, K. J. Friston, The functional anatomy of attention: a DCM study. *Front. Hum. Neurosci.* **7**,

784 (2013).

8. P. Kok, D. Rahnev, J. F. M. Jehee, H. C. Lau, F. P. de Lange, Attention Reverses the Effect of Prediction in Silencing Sensory Signals. *Cereb. Cortex* **22**, 2197–2206 (2011).

9. M. W. Spratling, Reconciling predictive coding and biased competition models of cortical function. *Front. Comput. Neurosci.* **2**, 4 (2008).

10. A. K. Seth, K. Suzuki, H. D. Critchley, An interoceptive predictive coding model of conscious presence. *Front. Psychol.* **3**, 395 (2012).

11. A. M. Bastos, W. M. Usrey, R. A. Adams, G. R. Mangun, P. Fries, K. J. Friston, Canonical microcircuits for predictive coding. *Neuron* **76**, 695–711 (2012).

12. K. Friston, A theory of cortical responses. *Philos. Trans. R. Soc. B Biol. Sci.* **360**, 815–836 (2005).

13. K. J. Friston, T. Parr, B. de Vries, The graphical brain: belief propagation and active inference. *Netw. Neurosci.*, 1–78 (2017).

14. M. W. Spratling, Predictive coding as a model of response properties in cortical area V1. *J. Neurosci. Off. J. Soc. Neurosci.* **30**, 3531–3543 (2010).

15. S. S. Solomon, H. Tang, E. Sussman, A. Kohn, Limited evidence for sensory prediction error responses in visual cortex of macaques and humans. *Cereb. Cortex* **31**, 3136–3152 (2021).

16. Y. (Sophy) Xiong, J. A. Donoghue, M. Lundqvist, M. Mahnke, A. J. Major, E. N. Brown, E. K. Miller, A. M. Bastos, Propofol-mediated loss of consciousness disrupts predictive routing and local field phase modulation of neural activity. *Proc. Natl. Acad. Sci.* **121**, e2315160121 (2024).

17. S. Furutachi, A. D. Franklin, A. M. Aldea, T. D. Mrsic-Flogel, S. B. Hofer, Cooperative thalamocortical circuit mechanism for sensory prediction errors. *Nature* **633**, 398–406 (2024).

18. S. Jamali, S. Bagur, E. Brémont, T. V. Kerkoerle, S. Dehaene, B. Bathellier, Parallel mechanisms signal a hierarchy of sequence structure violations in the auditory cortex. bioRxiv [Preprint] (2024). https://doi.org/10.1101/2024.08.21.609026.

19. G. Bastos, J. T. Holmes, J. M. Ross, A. M. Rader, C. G. Gallimore, J. A. Wargo, D. S. Peterka, J. P. Hamm, Top-down input modulates visual context processing through an interneuron-specific circuit. *Cell Rep.* **42**, 113133 (2023).

20. K. M. Gabhart, Y. (Sophy) Xiong, A. M. Bastos, Predictive coding: a more cognitive process than we thought? *Trends Cogn. Sci.* **0** (2025).

21. T. A. Bekinschtein, S. Dehaene, B. Rohaut, F. Tadel, L. Cohen, L. Naccache, Neural signature of the conscious processing of auditory regularities. *Proc. Natl. Acad. Sci.* **106**, 1672–1677 (2009).

22. V. A. Lamme, P. R. Roelfsema, The distinct modes of vision offered by feedforward and recurrent processing. *Trends Neurosci.* **23**, 571–579 (2000).

23. J. H. Siegle, X. Jia, S. Durand, S. Gale, C. Bennett, N. Graddis, G. Heller, T. K. Ramirez, H. Choi, J. A. Luviano, P. A. Groblewski, R. Ahmed, A. Arkhipov, A. Bernard, Y. N. Billeh, D. Brown, M. A. Buice, N. Cain, S. Caldejon, L. Casal, A. Cho, M. Chvilicek, T. C. Cox, K. Dai, D. J. Denman, S. E. J. de Vries, R. Dietzman, L. Esposito, C. Farrell, D. Feng, J. Galbraith, M. Garrett, E. C. Gelfand, N. Hancock, J. A.

Harris, R. Howard, B. Hu, R. Hytnen, R. Iyer, E. Jessett, K. Johnson, I. Kato, J. Kiggins, S. Lambert, J. Lecoq, P. Ledochowitsch, J. H. Lee, A. Leon, Y. Li, E. Liang, F. Long, K. Mace, J. Melchior, D. Millman, T. Mollenkopf, C. Nayan, L. Ng, K. Ngo, T. Nguyen, P. R. Nicovich, K. North, G. K. Ocker, D. Ollerenshaw, M. Oliver, M. Pachitariu, J. Perkins, M. Reding, D. Reid, M. Robertson, K. Ronellenfitch, S. Seid, C. Slaughterbeck, M. Stoecklin, D. Sullivan, B. Sutton, J. Swapp, C. Thompson, K. Turner, W. Wakeman, J. D. Whitesell, D. Williams, A. Williford, R. Young, H. Zeng, S. Naylor, J. W. Phillips, R. C. Reid, S. Mihalas, S. R. Olsen, C. Koch, Survey of spiking in the mouse visual system reveals functional hierarchy. *Nature* **592**, 86–92 (2021).

24. N. T. Markov, J. Vezoli, P. Chameau, A. Falchier, R. Quilodran, C. Huissoud, C. Lamy, P. Misery, P. Giroud, S. Ullman, P. Barone, C. Dehay, K. Knoblauch, H. Kennedy, The anatomy of hierarchy: Feedforward and feedback pathways in macaque visual cortex. *J. Comp. Neurol.*, doi: 10.1002/cne.23458 (2013).

25. B. Sotomayor-Gómez, F. P. Battaglia, M. Vinck, Firing rates in visual cortex show representational drift, while temporal spike sequences remain stable. *Cell Rep.* **44** (2025).

26. E. Maris, R. Oostenveld, Nonparametric statistical testing of EEG- and MEG-data. *J. Neurosci. Methods* **164**, 177–190 (2007).

27. J. P. Gavornik, M. F. Bear, Learned spatiotemporal sequence recognition and prediction in primary visual cortex. *Nat. Neurosci.* **17**, 732–737 (2014).

28. D. J. Felleman, D. C. Van Essen, Distributed hierarchical processing in the primate cerebral cortex. *Cereb. Cortex* **1**, 1–47 (1991).

29. M. Dhamala, G. Rangarajan, M. Ding, Estimating Granger Causality from Fourier and Wavelet Transforms of Time Series Data. *Phys. Rev. Lett.* **100**, 018701 (2008).

30. A. G. Nedungadi, G. Rangarajan, N. Jain, M. Ding, Analyzing multiple spike trains with nonparametric granger causality. *J. Comput. Neurosci.* **27**, 55–64 (2009).

31. J. Dimidschstein, Q. Chen, R. Tremblay, S. L. Rogers, G.-A. Saldi, L. Guo, Q. Xu, R. Liu, C. Lu, J. Chu, J. S. Grimley, A.-R. Krostag, A. Kaykas, M. C. Avery, M. S. Rashid, M. Baek, A. L. Jacob, G. B. Smith, D. E. Wilson, G. Kosche, I. Kruglikov, T. Rusielewicz, V. C. Kotak, T. M. Mowery, S. A. Anderson, E. M. Callaway, J. S. Dasen, D. Fitzpatrick, V. Fossati, M. A. Long, S. Noggle, J. H. Reynolds, D. H. Sanes, B. Rudy, G. Feng, G. Fishell, A viral strategy for targeting and manipulating interneurons across vertebrate species. *Nat. Neurosci.* **19**, 1743–1749 (2016).

32. S. Torres-Gomez, J. D. Blonde, D. Mendoza-Halliday, E. Kuebler, M. Everest, X. J. Wang, W. Inoue, M. O. Poulter, J. Martinez-Trujillo, Changes in the Proportion of Inhibitory Interneuron Types from Sensory to Executive Areas of the Primate Neocortex: Implications for the Origins of Working Memory Representations. *Cereb. Cortex* **30**, 4544–4562 (2020).

33. A. M. Bastos, W. M. Usrey, R. A. Adams, G. R. Mangun, P. Fries, K. J. Friston, Canonical Microcircuits for Predictive Coding. *Neuron* **76**, 695–711 (2012).

34. N. Qian, J. Zhang, Neuronal Firing Rate As Code Length: a Hypothesis. *Comput. Brain Behav.* **3**, 34–53 (2020).

35. M. E. Bellet, M. Gay, J. Bellet, B. Jarraya, S. Dehaene, T. van Kerkoerle, T. I. Panagiotaropoulos, Spontaneously emerging internal models of visual sequences combine abstract and event-specific information in the prefrontal cortex. *Cell Rep.* **43** (2024).

36. A. D. Huberman, M. B. Feller, B. Chapman, Mechanisms Underlying Development of Visual Maps and Receptive Fields. *Annu. Rev. Neurosci.* **31**, 479–509 (2008).

37. M. Rigotti, O. Barak, M. R. Warden, X.-J. Wang, N. D. Daw, E. K. Miller, S. Fusi, The importance of mixed selectivity in complex cognitive tasks. *Nature* **497**, 585–590 (2013).

38. K. Hoemann, L. and Feldman Barrett, Concepts dissolve artificial boundaries in the study of emotion and cognition, uniting body, brain, and mind. *Cogn. Emot.* **33**, 67–76 (2019).

39. K. M. Tye, E. K. Miller, F. H. Taschbach, M. K. Benna, M. Rigotti, S. Fusi, Mixed selectivity: Cellular computations for complexity. *Neuron* **112**, 2289–2303 (2024).

40. E. K. Miller, M. Lundqvist, A. M. Bastos, Working Memory 2.0. *Neuron* **100**, 463–475 (2018).

41. A. M. Bastos, M. Lundqvist, A. S. Waite, N. Kopell, E. K. Miller, Layer and rhythm specificity for predictive routing. *Proc. Natl. Acad. Sci. U. S. A.* **117**, 31459–31469 (2020).

42. R. F. Salazar, N. M. Dotson, S. L. Bressler, C. M. Gray, Content-specific fronto-parietal synchronization during visual working memory. *Science* **338**, 1097–1100 (2012).

43. J. H. Marshel, Y. S. Kim, T. A. Machado, S. Quirin, B. Benson, J. Kadmon, C. Raja, A. Chibukhchyan, C. Ramakrishnan, M. Inoue, J. C. Shane, D. J. McKnight, S. Yoshizawa, H. E. Kato, S. Ganguli, K. Deisseroth, Cortical layer–specific critical dynamics triggering perception. *Science* **365**, eaaw5202 (2019).

44. S. Durand, G. R. Heller, T. K. Ramirez, J. A. Luviano, A. Williford, D. T. Sullivan, A. J. Cahoon, C. Farrell, P. A. Groblewski, C. Bennett, J. H. Siegle, S. R. Olsen, Acute head-fixed recordings in awake mice with multiple Neuropixels probes. *Nat. Protoc.* **18**, 424–457 (2023).

45. A. L. Juavinett, I. Nauhaus, M. E. Garrett, J. Zhuang, E. M. Callaway, Automated identification of mouse visual areas with intrinsic signal imaging. *Nat. Protoc.* **12**, 32–43 (2017).

46. J. H. Siegle, A. C. López, Y. A. Patel, K. Abramov, S. Ohayon, J. Voigts, Open Ephys: an open-source, plugin-based platform for multichannel electrophysiology. *J. Neural Eng.* **14**, 045003 (2017).

47. A. Mathis, P. Mamidanna, K. M. Cury, T. Abe, V. N. Murthy, M. W. Mathis, M. Bethge, DeepLabCut: markerless pose estimation of user-defined body parts with deep learning. *Nat. Neurosci.* **21**, 1281–1289 (2018).

48. M. Pachitariu, S. Sridhar, C. Stringer, Solving the spike sorting problem with Kilosort. bioRxiv [Preprint] (2023). https://doi.org/10.1101/2023.01.07.523036.

49. O. Rübel, A. Tritt, R. Ly, B. K. Dichter, S. Ghosh, L. Niu, P. Baker, I. Soltesz, L. Ng, K. Svoboda, L. Frank, K. E. Bouchard, The Neurodata Without Borders ecosystem for neurophysiological data science. *eLife* **11**, e78362 (2022).

50. S. Q. Lima, T. Hromádka, P. Znamenskiy, A. M. Zador, PINP: A New Method of Tagging Neuronal Populations for Identification during In Vivo Electrophysiological Recording. *PLOS ONE* **4**, e6099 (2009).

51. U. Mitzdorf, Current source-density method and application in cat cerebral cortex: investigation of evoked potentials and EEG phenomena. *Physiol. Rev.* **65**, 37–100 (1985).

52. C. Nicholson, J. A. Freeman, Theory of current source-density analysis and determination of conductivity tensor for anuran cerebellum. *J. Neurophysiol.* **38**, 356–368 (1975).

53. U. Mitzdorf, W. Singer, Prominent excitatory pathways in the cat visual cortex (A 17 and A 18): A current source density analysis of electrically evoked potentials. *Exp. Brain Res.* **33**, 371–394 (1978).

54. A. Maier, G. Adams, C. Aura, D. Leopold, Distinct Superficial and Deep Laminar Domains of Activity in the Visual Cortex during Rest and Stimulation. *Front. Syst. Neurosci.* **4** (2010).

55. D. Mendoza-Halliday, A. J. Major, N. Lee, M. J. Lichtenfeld, B. Carlson, B. Mitchell, P. D. Meng, Y. S. Xiong, J. A. Westerberg, X. Jia, K. D. Johnston, J. Selvanayagam, S. Everling, A. Maier, R. Desimone, E. K. Miller, A. M. Bastos, A ubiquitous spectrolaminar motif of local field potential power across the primate cortex. *Nat. Neurosci.* **27**, 547–560 (2024).

56. D. A. Tovar, J. A. Westerberg, M. A. Cox, K. Dougherty, M. T. Wallace, A. M. Bastos, A. Maier, Near-field potentials index local neural computations more accurately than population spiking. bioRxiv [Preprint] (2023). https://doi.org/10.1101/2023.05.11.540026.

57. D. A. Tovar, J. A. Westerberg, M. A. Cox, K. Dougherty, T. A. Carlson, M. T. Wallace, A. Maier, Stimulus Feature-Specific Information Flow Along the Columnar Cortical Microcircuit Revealed by Multivariate Laminar Spiking Analysis. *Front. Syst. Neurosci.* **14** (2020).

58. J. A. Westerberg, M. A. Cox, K. Dougherty, A. Maier, V1 microcircuit dynamics: altered signal propagation suggests intracortical origins for adaptation in response to visual repetition. *J. Neurophysiol.* **121**, 1938–1952 (2019).

59. N. K. Logothetis, J. Pauls, M. Augath, T. Trinath, A. Oeltermann, Neurophysiological investigation of the basis of the fMRI signal. *Nature* **412**, 150–157 (2001).

60. M. W. Self, T. van Kerkoerle, H. Supèr, P. R. Roelfsema, Distinct Roles of the Cortical Layers of Area V1 in Figure-Ground Segregation. *Curr. Biol.* **23**, 2121–2129 (2013).

61. H. Supèr, P. R. Roelfsema, Chronic multiunit recordings in behaving animals: advantages and limitations. *Prog. Brain Res.* **147**, 263–282 (2005).

62. E. M. Trautmann, S. D. Stavisky, S. Lahiri, K. C. Ames, M. T. Kaufman, D. J. O'Shea, S. Vyas, X. Sun, S. I. Ryu, S. Ganguli, K. V. Shenoy, Accurate Estimation of Neural Population Dynamics without Spike Sorting. *Neuron* **103**, 292-308.e4 (2019).

63. J. A. Westerberg, J. D. Schall, G. F. Woodman, A. Maier, Feedforward attentional selection in sensory cortex. *Nat. Commun.* **14**, 5993 (2023).

64. J. A. Westerberg, A. Maier, J. D. Schall, Priming of Attentional Selection in Macaque Visual Cortex: Feature-Based Facilitation and Location-Based Inhibition of Return. *eNeuro* **7** (2020).

65. R. O. R. Y. Thompson, Coherence Significance Levels. *J. Atmospheric Sci.* **36**, 2020–2021 (1979).

66. J. Hwang, A. R. Mitz, E. A. Murray, NIMH MonkeyLogic: Behavioral control and data acquisition in MATLAB. *J. Neurosci. Methods* **323**, 13–21 (2019).

67. M. J. Lichtenfeld, A. G. Mulvey, H. Nejat, Y. S. Xiong, B. M. Carlson, B. A. Mitchell, D. Mendoza-Halliday, J. A. Westerberg, R. Desimone, A. Maier, J. H. Kaas, A. M. Bastos, The laminar organization of cell types in macaque cortex and its relationship to neuronal oscillations. *bioRxiv*, 2024.03.27.587084 (2024).

68. R. Oostenveld, P. Fries, E. Maris, J.-M. Schoffelen, FieldTrip: Open source software for advanced analysis of MEG, EEG, and invasive electrophysiological data. *Comput. Intell. Neurosci.* **2011**, 156869

(2011).

69. J. A. Harris, S. Mihalas, K. E. Hirokawa, J. D. Whitesell, H. Choi, A. Bernard, P. Bohn, S. Caldejon, L. Casal, A. Cho, A. Feiner, D. Feng, N. Gaudreault, C. R. Gerfen, N. Graddis, P. A. Groblewski, A. M. Henry, A. Ho, R. Howard, J. E. Knox, L. Kuan, X. Kuang, J. Lecoq, P. Lesnar, Y. Li, J. Luviano, S. McConoughey, M. T. Mortrud, M. Naeemi, L. Ng, S. W. Oh, B. Ouellette, E. Shen, S. A. Sorensen, W. Wakeman, Q. Wang, Y. Wang, A. Williford, J. W. Phillips, A. R. Jones, C. Koch, H. Zeng, Hierarchical organization of cortical and thalamic connectivity. *Nature* **575**, 195–202 (2019).

70. M. A. Cox, K. Dougherty, J. A. Westerberg, M. S. Schall, A. Maier, Temporal dynamics of binocular integration in primary visual cortex. *J. Vis.* **19**, 13 (2019).

71. D. C. Godlove, A. Maier, G. F. Woodman, J. D. Schall, Microcircuitry of Agranular Frontal Cortex: Testing the Generality of the Canonical Cortical Microcircuit. *J. Neurosci.* **34**, 5355–5369 (2014).

72. Y. Kajikawa, J. F. Smiley, C. E. Schroeder, Primary Generators of Visually Evoked Field Potentials Recorded in the Macaque Auditory Cortex. *J. Neurosci.* **37**, 10139–10153 (2017).

73. A. Maier, C. J. Aura, D. A. Leopold, Infragranular Sources of Sustained Local Field Potential Responses in Macaque Primary Visual Cortex. *J. Neurosci.* **31**, 1971–1980 (2011).

74. A. D. Mehta, I. Ulbert, C. E. Schroeder, Intermodal selective attention in monkeys. I: distribution and timing of effects across visual areas. *Cereb. Cortex* **10**, 343–358 (2000).

75. A. D. Mehta, I. Ulbert, C. E. Schroeder, Intermodal Selective Attention in Monkeys. II: Physiological Mechanisms of Modulation. *Cereb. Cortex* **10**, 359–370 (2000).

76. T. Ninomiya, K. Dougherty, D. C. Godlove, J. D. Schall, A. Maier, Microcircuitry of agranular frontal cortex: contrasting laminar connectivity between occipital and frontal areas. *J. Neurophysiol.* **113**, 3242–3255 (2015).

77. C. E. Schroeder, A. D. Mehta, S. J. Givre, A spatiotemporal profile of visual system activation revealed by current source density analysis in the awake macaque. *Cereb. Cortex* **8**, 575–592 (1998).

78. T. van Kerkoerle, M. W. Self, P. R. Roelfsema, Layer-specificity in the effects of attention and working memory on activity in primary visual cortex. *Nat. Commun.* **8**, 13804 (2017).

79. T. van Kerkoerle, M. W. Self, B. Dagnino, M.-A. Gariel-Mathis, J. Poort, C. van der Togt, P. R. Roelfsema, Alpha and gamma oscillations characterize feedback and feedforward processing in monkey visual cortex. *Proc. Natl. Acad. Sci.* **111**, 14332–14341 (2014).

80. J. A. Westerberg, M. S. Schall, A. Maier, G. F. Woodman, J. D. Schall, Laminar microcircuitry of visual cortex producing attention-associated electric fields. *eLife* **11**, e72139 (2022).

81. J. A. Westerberg, E. A. Sigworth, J. D. Schall, A. Maier, Pop-out search instigates beta-gated feature selectivity enhancement across V4 layers. *Proc. Natl. Acad. Sci.* **118** (2021).

82. B. Herrera, J. A. Westerberg, M. S. Schall, A. Maier, G. F. Woodman, J. D. Schall, J. J. Riera, Resolving the mesoscopic missing link: Biophysical modeling of EEG from cortical columns in primates. *NeuroImage* **263**, 119593 (2022).

83. K. V. Nourski, M. Steinschneider, A. E. Rhone, H. Kawasaki, M. A. Howard, M. I. Banks, Auditory Predictive Coding across Awareness States under Anesthesia: An Intracranial Electrophysiology Study. *J.*

Neurosci. **38**, 8441–8452 (2018).

84. S. J. Kiebel, J. Daunizeau, K. J. Friston, A Hierarchy of Time-Scales and the Brain. *PLoS Comput. Biol.* **4**, e1000209 (2008).

85. J. L. Barbur, A. J. Harlow, A. Sahraie, Pupillary responses to stimulus structure, colour and movement. *Ophthalmic Physiol. Opt.* **12**, 137–141 (1992).

86. C. G. Gallimore, D. A. Ricci, J. P. Hamm, Spatiotemporal dynamics across visual cortical laminae support a predictive coding framework for interpreting mismatch responses. *Cereb. Cortex* **33**, 9417–9428 (2023).

87. C. Wacongne, E. Labyt, V. van Wassenhove, T. Bekinschtein, L. Naccache, S. Dehaene, Evidence for a hierarchy of predictions and prediction errors in human cortex. *Proc. Natl. Acad. Sci.* **108**, 20754–20759 (2011).

88. C. Wacongne, J.-P. Changeux, S. Dehaene, A Neuronal Model of Predictive Coding Accounting for the Mismatch Negativity. *J. Neurosci.* **32**, 3665–3678 (2012).

89. N. Nitzan, G. Buzsáki, Diversity of omission responses to visual images across brain-wide regions. *Sci. Adv.* **11**, eadv5651 (2025).

90. A. Maier, N. Tsuchiya, Growing evidence for separate neural mechanisms for attention and consciousness. *Atten. Percept. Psychophys.* **83**, 558–576 (2021).

91. H. Feldman, K. J. Friston, Attention, uncertainty, and free-energy. *Front. Hum. Neurosci.* **4**, 215 (2010).

92. W. M. Bolstad, J. M. Curran, *Introduction to Bayesian Statistics* (Wiley, Hoboken, New Jersey, Third edition., 2017).

Acknowledgments

The Neuropixels dataset was obtained at the Allen Brain Observatory as part of the OpenScope program, which is operated by the Allen Institute, Neural Dynamics. We thank the OpenScope steering committee for their support and the Allen Institute founder, Paul G. Allen, for his vision, encouragement, and support.

Funding

National Institutes of Health [grant number: R00MH116100] (AMB)

National Institutes of Health [grant number: U24NS113646] (JAL)

Vanderbilt Brain Institute Faculty Fellow Award (AMB)

Vanderbilt University Startup Funds (AMB)

International Human Frontier Science Program Organization [grant number: LT0001/2023-L] (JAW)

Dutch Research Council [grant number: VI.Veni.232.110] (JAW)

Author contributions

Conceptualization: JAW, AM, AMB

Data curation: JAW, AB, SD, BH, JAL

Formal analysis: JAW, YSX, ES, AMB

Funding acquisition: JAW, JAL, AMB

Investigation (NHP studies): JAW, YSX, HN, AMB

Investigation (rodent studies): SD, BH, HC, HB, HL, WH, KN, VH, TJ, CG, AY, JS, RG, BO, SC, AW, PAG

Project administration: JAW, CK, JAL, AM, AMB

Software: JAW, AB, CRP

Supervision: SRO, JAL, AM, AMB

Validation: JAW, AB, CRP, JAL

Visualization: JAW, YSX

Writing – original draft: JAW, AM, AMB

Writing – review, and editing: all authors

Competing interests

Authors declare that they have no competing interests.

Data and materials availability

All mouse data used in this work are openly available through the DANDI Archive (dandiset id: 000253, doi: https://doi.org/10.48324/dandi.000253/0.240503.0152). Software resources for the analysis of this dataset are provided here: https://alleninstitute.github.io/openscope_databook/projects/glo.html. The

code to generate the global-local oddball sequences is provided here: https://github.com/AllenInstitute/openscope-glo-stim.

Supplementary Materials

Materials and Methods

Supplementary Text

Figs. S1-S11

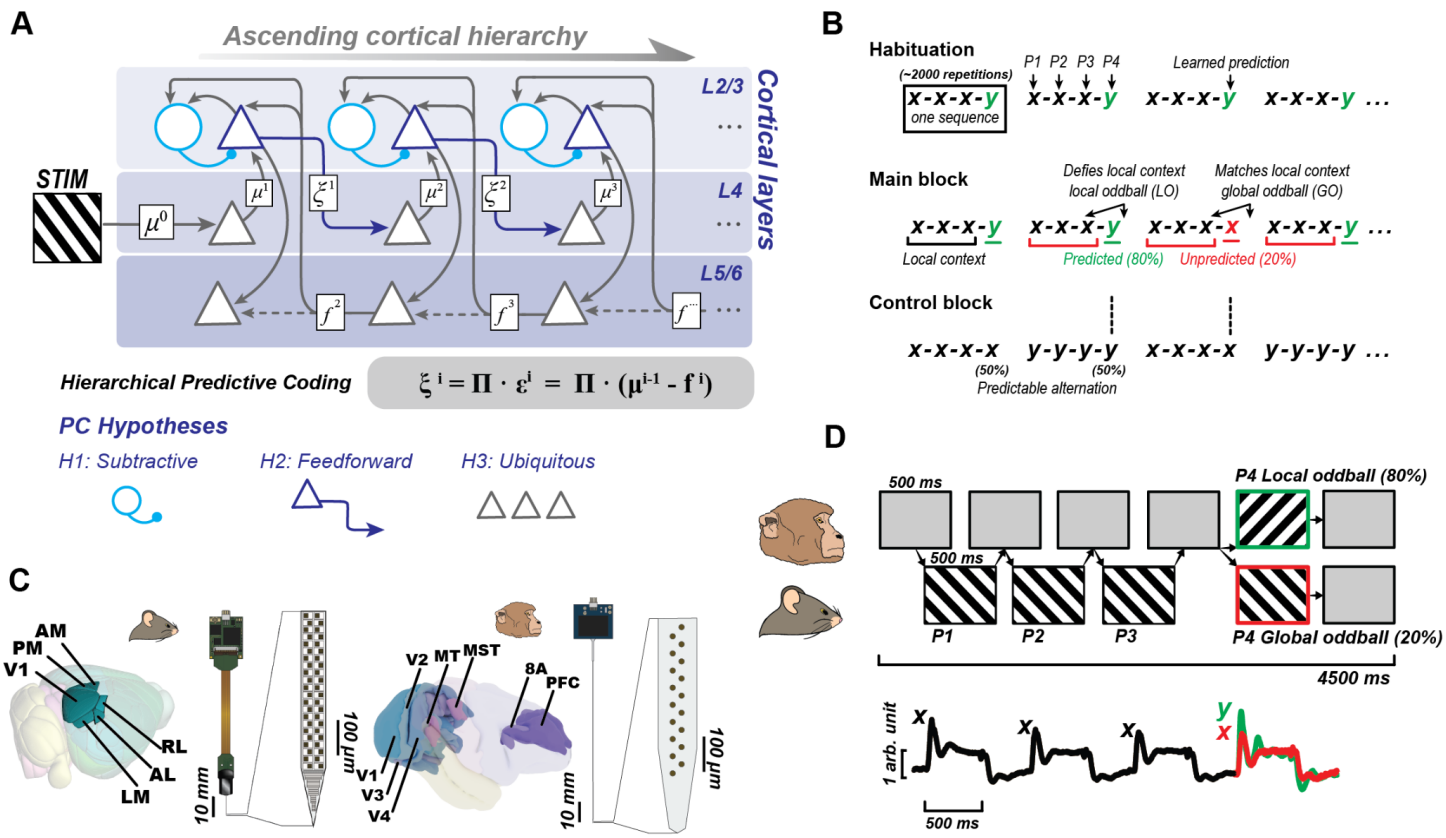

Fig. 1 Predictive Coding (PC) hypotheses, Local/global oddball paradigm, and experimental setup. (A) Schematic for sensory processing via hierarchical predictive coding. Stimulus information enters the cortical hierarchy through layer 4, and prediction error is computed in superficial layers 2/3, with inhibitory cell involvement in the subtractive process (H1). Prediction error is then fed forward (H2) via superficial layers to higher-order areas. Higher-order areas provide a feedback prediction from deep layers. Error signals emerge early and propagate throughout cortical hierarchy (H3) (B) Visual stimuli were presented in 4-stimulus sequences consisting of 2-oriented, drifting gratings symbolized as 'x' or 'y'. Animals were extensively habituated to the predictable x-x-x-y sequence (counterbalanced over sessions/animals with y-y-y-x). In the main block of a recording session animals were presented with 80% x-x-x-y and 20% x-x-x-x (global oddballs). Control blocks consisted of x-x-x-x (control for global oddball, 50% of trials) and y-y-y-y (control for local oddball, 50% of trials). (C) Neuropixels were introduced into 6 visual cortical regions in all mice (V1, LM, RL, AL, PM, AM). 128-channel or 32-channel laminar probes were introduced into 8 cortical regions in 2 monkeys (V1, V2, V3, V4, MT, MST, 8A, PFC). (D) Macaque monkeys viewed sequences of drifting grating stimuli while fixating centrally with a stimulus duration of 500 ms and inter-stimulus interval of 531ms. Mice viewed sequences of full-screen drifting grating stimuli with a duration of 500 ms with a 500 ms inter-stimulus interval and 1 s inter-trial intervals. Trace at bottom shows example population average response to the 4-stimulus sequences with the global oddball indicated in red and the local oddball in green.

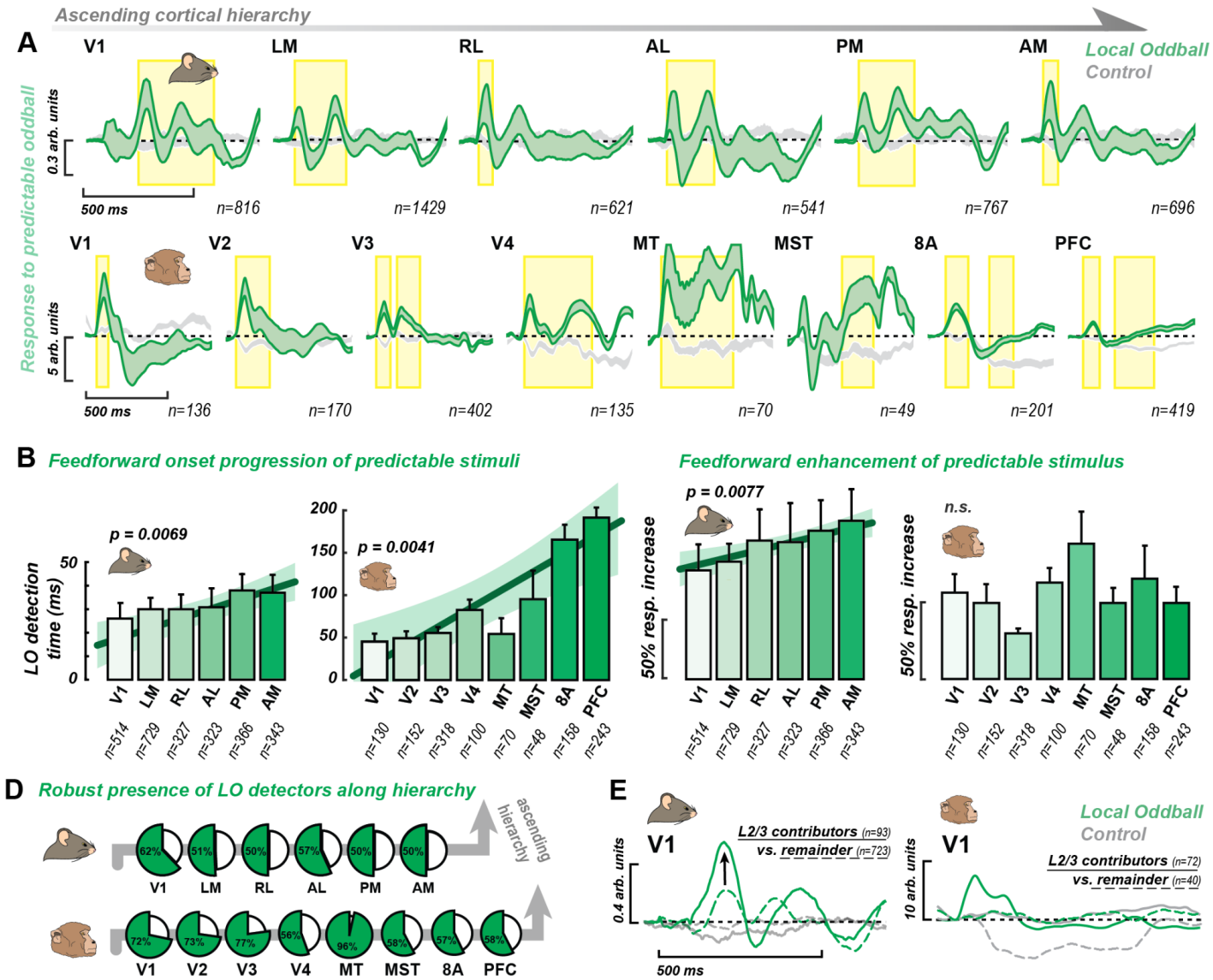

Fig. 2 Predictable local oddball is widespread, emerges early, and feeds forward. (A) Local oddball detection across cortical areas in mice and monkeys. Bands are 95% confidence intervals across units in an area. Unit responses are normalized by dividing instantaneous firing rate by average firing rate at the single-unit level in mice and via a z-score method for the multiunit data in monkeys (see *Materials and Methods*). Green bands are the P4-P3 local oddball in the main block; gray bands are the P4-P3 local oddball in the control block. For non-subtracted neuronal activity, see Fig. S7. Yellow highlights reflect significant population local oddball detection periods, P<0.05, corrected for multiple comparisons using nonparametric, cluster-based permutation tests. Local oddball signalling in mice was accompanied by a stimulus-induced temporal modulation corresponding to the drifting grating presentation rate of 4Hz (A, upper subpanel). This oscillatory component was much less prominent in monkeys (A, lower subpanel). (B) Average onset time for significant local oddball effect across hierarchy in mice and monkeys. Error bars indicate 2xSEM across cells/channels. Linear regression shows significant relationship between hierarchical position and onset timing (R^2 = 0.83, P=0.006 in mice; R^2 = 0.88, P= 0.004 in monkeys), indicating a feedforward progression. (C) Percent response increase to local oddball across cortical areas in mice and monkeys. Error bars indicate 2xSEM across cells/channels. Local oddball effects show significant feedforward enhancement in mice along the cortical hierarchy. (D) Percentage of local oddball encoding units/channels along cortical hierarchy in mice and monkeys. In both species, signaling of predictable local oddballs is robust (>50% of all cortical areas) and widespread (observed in all cortical areas) (E) Local oddball responses are more pronounced in L2/3 in V1 in both mice and monkeys compared to cell/channels in other layers, suggesting feedforward signaling.

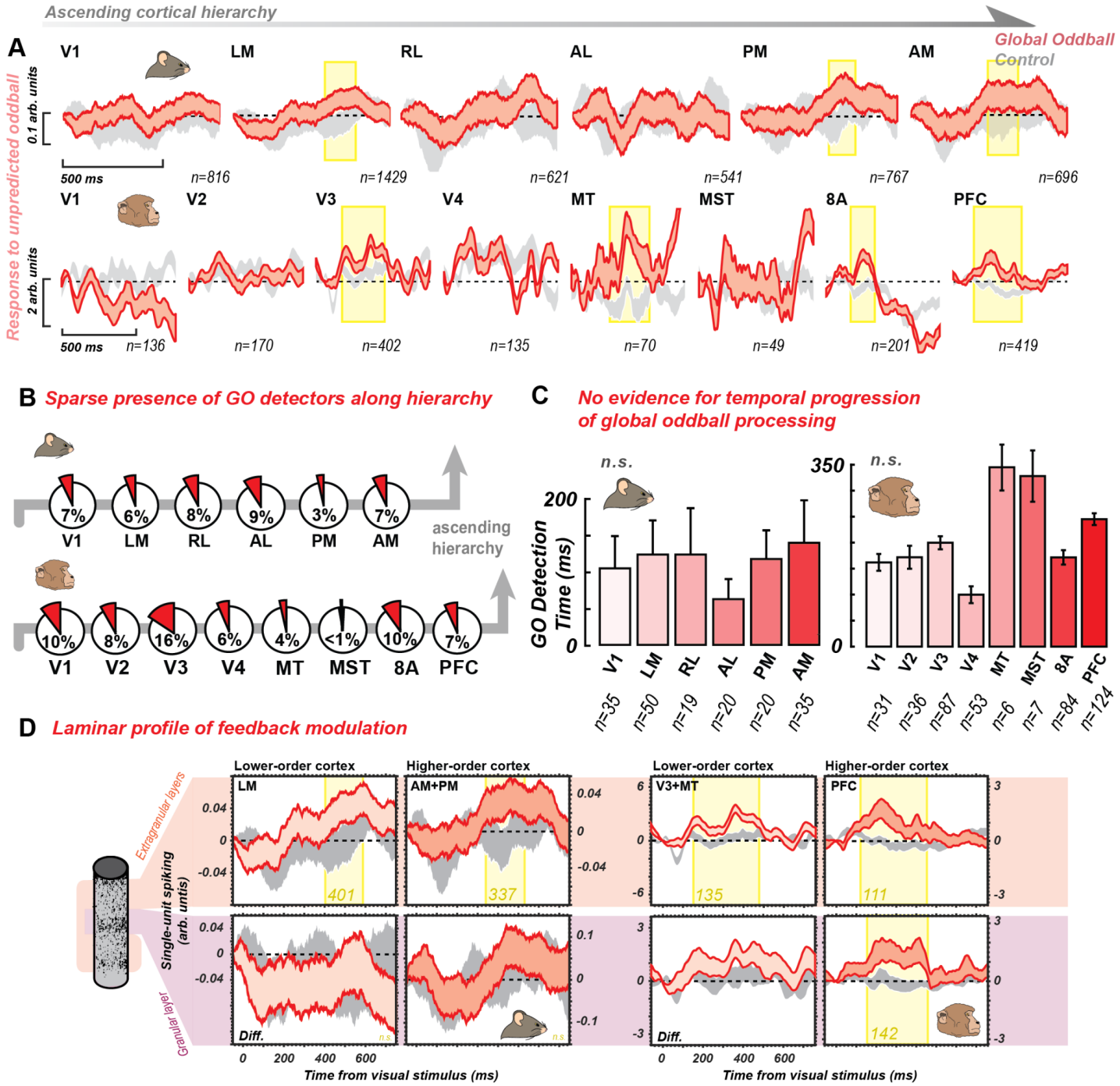

Fig. 3 Unpredictable global oddball emerges in higher-order cortex and is fed back. (A) Global oddball detection across cortical areas in mice and monkeys. Bands are 95% confidence intervals across units in an area. Red bands are P4-P3 in the GLO block; gray bands are P4-P3 in the control block. For non-subtracted neuronal activity, see Fig. S7. Yellow highlights reflect periods of significant population global oddball detection, P<0.05, corrected for multiple comparisons using nonparametric, cluster-based permutation tests. (B) Percentage of significant global oddball encoding units/channels along the cortical hierarchy in mice and monkey. (C) Onset times of significance for global oddball effect along the cortical hierarchy in mice and monkeys. Linear regressions show no significant change along cortical hierarchy, suggesting no strong feedforward signaling of global oddball prediction error. (D) Granular versus extra-granular global oddball detection in areas with significant population-level detection in mice and monkeys. Red bands are P4-P3 in the GLO block; gray bands are P4-P3 in the control block. Yellow highlights reflect periods of significant population global oddball detection in the layer grouping, with the latency indicated.

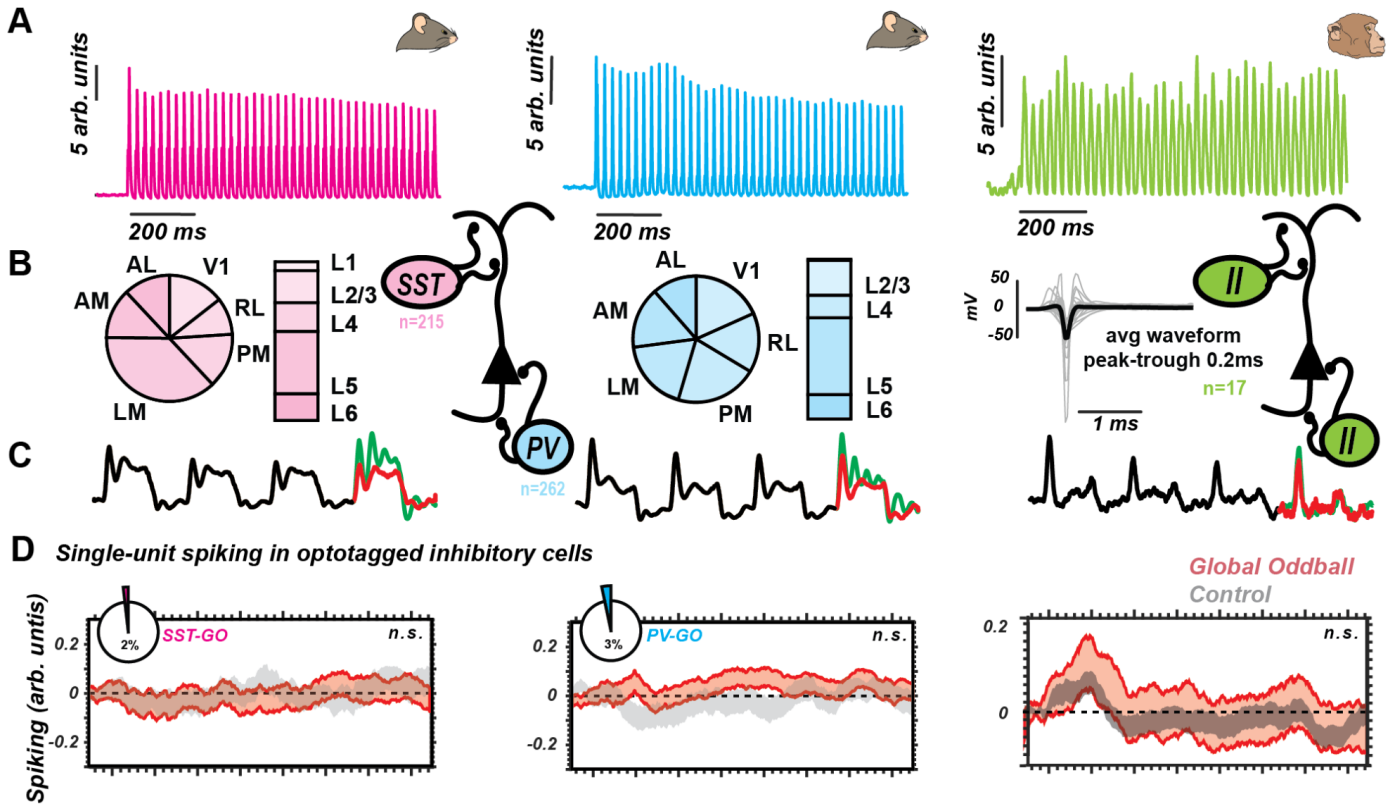

Fig. 4 Optogenetically identified inhibitory cells in mice and monkeys do not carry out hypothesized predictive coding functions. (A) Optical stimulation with 40 Hz sinusoidal modulation of laser power. Tagged SST (magenta, n=215 neurons) and PV (cyan, n=262 neurons) responses are normalized by their average firing rate. In primates, an opsin targeting all GABAergic inhibitory cells was used; responses shown were computed as a weighted mean (green, n=21 neurons), where each cell is weighted by its modulation strength (average firing rate change from baseline, divided by the sum of baseline and laser-timed response). (B) Relative proportion of each inhibitory interneuron type, which have synapses at largely different sites on pyramidal cells (schematized here), across areas and layers in mice (left and middle). Average waveform shape and spike width in primate data (right) are consistent with that of narrow-spiking interneurons. (C) Population average spiking response to the oddball sequences for these inhibitory interneurons. P1 to P3 in black, local oddball P4 in green, and global oddball P4 in red. (D) Lack of global oddball detection in SST and PV cell subpopulations in mice and in pan-inhibitory cell populations in monkeys. Bands are 95% confidence intervals across units. Top, the red band is P4-P3 in the main block; the gray band is P4-P3 in the control block. For P3 and P4 components before subtraction, see Fig. S7B.

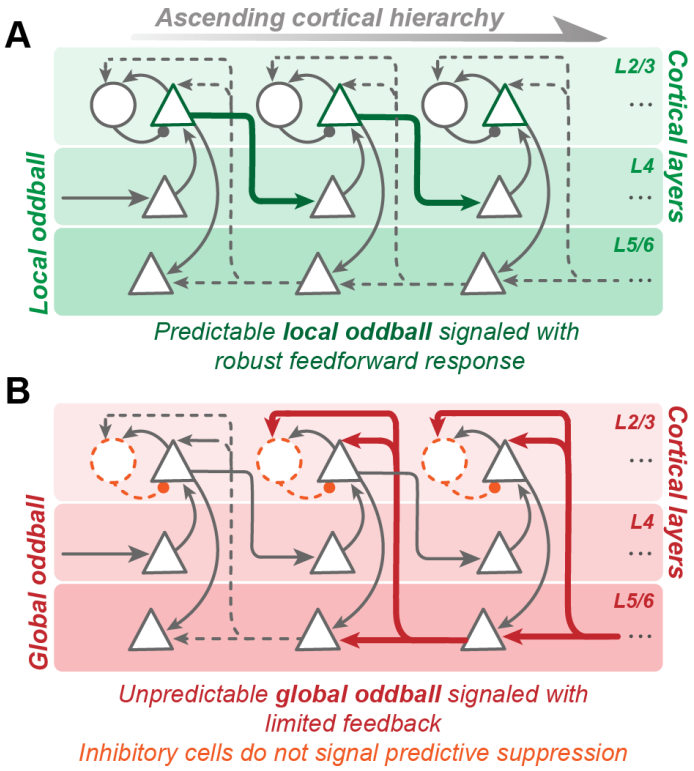

Fig. 5 Schematic of findings represented in the canonical cortical connections. (A) highly predictable local oddball resulted in robust and widespread feedforward response. The timings of onset of significance as well as granger causality results suggest strong feedforward processing. Thick green arrows represent strong cortical activity across layers and widespread across cortical hierarchy. (B) highly unpredictable global oddball resulted in limited feedback response, particularly in select higher order areas. We did not observe L2/3 prediction error signals in mice, and found non-specific L2/3 (compared to L5/6, except for in PFC at top of the hierarchy) prediction error signals in monkeys. Furthermore, optotagged inhibitory cells do not exhibit suppression specific to predictable stimuli.

Supplementary Materials

Materials and Methods

Mouse Experiments at the Allen Institute: Animals

All experiments were performed in 16 SSTAi32 and PVAi32 mice (*Mus musculus*) of both sexes (n_{male}=6, n_{female}=10), aged 95-128 days. Optogenetics experiments were conducted with Sst-IRES-Cre/wt; Ai32(RCL-ChR2(H134R)_EYFP)/wt mice (n=9) and Pvalb-IRES-Cre/wt; Ai32(RCL-ChR2(H134R)_EYFP)/wt) mice (n=7). Pvalb-IRES-Cre and Sst-IRES-Cre mice were bred in-house and crossed with an Ai32 channelrhodopsin reporter line. Pvalb-IRES-Cre;Ai32 breeding sets (pairs and trios) consisted of heterozygous Pvalb-IRES-Cre mice crossed with either heterozygous or homozygous Ai32(RCL-ChR2(H134R)_EYFP) mice. Pvalb-IRES-Cre is expressed in the male germline. To avoid germline deletion of the stop codon in the loxP-STOP-loxP cassette, Pvalb-IRES-Cre;Ai32 mice were not used as breeders. Sst-IRES-Cre;Ai32 breeding sets (pairs and trios) consisted of heterozygous Sst-IRES-Cre mice crossed with either heterozygous or homozygous Ai32(RCL-ChR2(H134R)_EYFP) mice. Cre+ cells from Ai32 lines are highly photosensitive, owing to the expression of Channelrhodopsin-2. All experiments on animals were conducted with the approval of the Allen Institute's Institutional Animal Care and Use Committee.

Macaque Monkey Experiments at Vanderbilt University: Animals

All procedures were approved by the Vanderbilt University Institutional Animal Care and Use Committee in compliance with the regulations set by the Association for the Assessment and Accreditation of Laboratory Animal Care and followed the United States National Institutes of Health guidelines. Two macaque monkeys were used in this study: one male adult bonnet macaque (*Macaca radiata*) aged 19 years (Ca, 7.4kg), and one male adult rhesus macaque (*Macaca mulatta*) aged 11 years (Jo, 12.0 kg).

Monkey Ca was injected with AAV vectors carrying an inhibitory cell-specific Dlx-ChR2-mCherry transgene. We mapped the planned trajectory of these injections with co-registered CT and MRI images. While the monkey was awake and head-fixed, we advanced an injectrode (32-channel Plexon V Probe customized with a fluid channel, Plexon, Dallas, TX) connected to a Hamilton syringe (Hamilton Company, Reno, NV) containing the viral vector in areas MT, MST, 8A, and PFC. Each injection site received 3 injections spaced 1mm apart in depth, starting from the deepest location. Injections are followed by a one-minute waiting period, after which the injectrode was retracted to the next injection depth. We injected in total 52.8μL of AAV1-Dlx-ChR2-mCherry and 13.2μL of AAV9-Dlx-ChR2-mCherry (9.6μL AAV1 and 2.4μL AAV9 in PFC, 19.2μL AAV1 and 4.8μL AAV9 in 8a, 14.4μL AAV1 and 3.6μL AAV9 in MT, 14.4μL AAV1 and 3.6μL AAV9 in MST). Each injection was confirmed by simultaneous recording of neuronal activity on nearby channels close to the fluid port, in which neuronal activity decreased during injections.

Mouse Experiments at the Allen Institute: Surgery

The surgery pipeline at the Allen Institute is described in detail in previous reports (*23*, *44*). Briefly, A pre-operative injection of dexamethasone (3.2 mg kg^{-1}, subcutaneously was administered 1 hr before surgery to

575 reduce swelling and postoperative pain by decreasing inflammation. Mice were initially anesthetized with 5%
576 isoflurane (1–3 min) and placed in a stereotaxic frame (Model 1900, Kopf). Isoflurane levels were maintained at
577 1.5–2.5% for the duration of the surgery. Body temperature was maintained at 37.5 °C. Carprofen was
578 administered for pain management (5–10 mg/kg, subcutaneous), and atropine was administered to suppress
579 bronchial secretions and regulate heart rhythm (0.02–0.05 mg/kg, subcutaneous). An incision was made to
580 remove the skin, and the exposed skull was leveled with respect to pitch (bregma–lambda level), roll, and yaw.
581 The headframe was placed on the skull and fixed with White C&B Metabond (Parkell). Once the Metabond was
582 dry, the mouse was placed in a custom clamp to position the skull at a rotated angle of 20° to facilitate the
583 creation of the craniotomy over the visual cortex. A circular piece of skull 5 mm in diameter was removed, and
584 a durotomy was performed. The brain was covered by a 5-mm-diameter circular glass coverslip, with a 1-mm
585 lip extending over the intact skull. The bottom of the coverslip was coated with a layer of polydimethylsiloxane
586 (SYLGARD 184, Sigma-Aldrich) to reduce adhesion to the brain surface. The coverslip was secured to the
587 skull with Vetbond (Patterson Veterinary). Kwik-Cast (World Precision Instruments) was added around the
588 coverslip to further seal the implant, and Metabond bridges between the coverslip and the headframe well were
589 created to hold the Kwik-Cast in place. At the end of the procedure, but before recovery from anesthesia, the
590 mouse was transferred to a photodocumentation station to capture a spatially registered image of the cranial
591 window.

592 Intrinsic signal imaging was performed to identify visual area boundaries (*45*). An insertion window was
593 designed for each mouse based on the identified visual areas. Mice were habituated to head fixation and visual
594 stimulation over two weeks.

595 <u>Macaque monkey experiments at Vanderbilt University: Surgery</u>

596 Monkeys were implanted with a headpost and recording chambers during an anesthetized procedure. Monkeys
597 were anesthetized with isoflurane. Body temperature was maintained near 38°C with a circulating water or
598 warm air recirculating heating blanket. Peripheral oxygen levels, heart rate, temperature, ECG, and expired
599 CO2 levels were monitored continuously during surgery. After mounting the animal in a stereotaxic device, the
600 animal's head was shaved and scrubbed (with Betadine and ethanol). Local anesthetic (Lidocaine) was injected
601 subcutaneously before opening and also placed into the ear canals before fitting the animal into the stereotaxic
602 device.

603 A skin flap was made over the skull. The skull was cleaned and dried, and orthopedic screws were placed in the
604 skull. The head restraint device, held in position with a stereotaxic holder, was fixed in place with orthopedic
605 screws and methyl methacrylate cement. Custom-made recording chambers (~20 mm in diameter, Crist
606 Instruments) were placed on the skull to allow access to all targeted brain areas in one hemisphere and secured
607 in place with orthopedic screws and dental cement. Craniotomies (10-20 mm diameter) were subsequently
608 performed using piezosurgery drills (Piezosurgery, Columbus, Ohio) to permit access to the underlying cortex.
609 Monkey Ca had two recording chambers, one placed over the prefrontal cortex (giving access to areas FEF and
610 LPFC) and one placed over the temporal cortex (giving access to areas MT, MST, V4, and TEO). Monkey Jo
611 had one recording chamber positioned over the occipital cortex (giving access to areas V1, V2, and V3). After
612 surgery, analgesics were given for pain management (Buprenorphine and NSAIDs for 3 days), and animals
613 showed no signs of pain or distress.

614 Mouse Experiments at the Allen Institute: Electrophysiology Experiments

615 The Neuropixels data was acquired at the Allen Institute as part of the OpenScope project that allows the
616 community to apply for observation on the Allen Brain Observatory platform
617 (https://alleninstitute.org/division/mindscope/openscope/). The Neuropixels pipeline at the Allen Institute is
618 described in detail in previous reports (*23*, *44*).

619 On the day of recording, the cranial coverslip was removed and replaced with the insertion window containing
620 holes aligned to six cortical visual areas. Mice were allowed to recover for 1–2 hours after the window was
621 placed before being head-fixed in the recording rig.

622 Six Neuropixels probes were targeted to each of the six visual cortical areas (V1, LM, RL, AL, PM, AM). The
623 boundaries of these areas and their retinotopic maps were obtained through intrinsic signal imaging, and
624 insertion locations were planned to target regions responsive to the center of the LCD monitor. Probes were
625 doused with CM-DiI (1 mM in ethanol; Thermo Fisher, V22888) for post hoc ex vivo probe localization. Each
626 probe was mounted on a 3-axis micromanipulator (New Scale Technologies). The tip of each probe was aligned
627 to its associated opening in the insertion window using a coordinate transformation obtained via a previous
628 calibration procedure. XYZ manipulator coordinates were obtained via a previous calibration procedure where
629 the tips of probes were aligned to the retinotopic centers of target visual areas using an image provided by
630 intrinsic signal imaging. The operator then moved each probe into place with a joystick, with the probes fully
631 retracted along the insertion axis, approximately 2.5 mm above the brain surface. The probes were manually
632 lowered to the brain surface until spikes were visible on the electrodes closest to the tip. After the probes
633 penetrated the brain to a depth of around 100 μm, they were inserted automatically at a rate of 200 μm/min
634 (total of 3.5 mm or less in the brain). After the probes reached their targets, they were allowed to settle for 5–10
635 min.

636 Neuropixels data was acquired at 30 kHz (spike band, 500 Hz high-pass filter) and 2.5 kHz (LFP band, 1,000
637 Hz low-pass filter) using the Open Ephys GUI (*46*). Videos of the eye and body were acquired at 60 Hz. Pupil
638 size was measured via previously described means (*23*). Briefly, a universal eye tracking model trained in
639 DeepLabCut (*47*), a ResNET-50-based network, recognizes up to 12 tracking points each around the perimeter
640 of the eye, the pupil, and the corneal reflection. The angular velocity of the running wheel was recorded at the
641 time of each stimulus frame, at approximately 60 Hz.

642 The spike-band data was median-subtracted, first within-channel to center the signal around zero, then across
643 channels to remove common-mode noise. The median-subtracted data file was sent through the Kilosort2
644 MATLAB package (https://github.com/mouseland/Kilosort2) (*48*), which applies a 150 Hz high-pass filter,
645 followed by whitening in blocks of 32 channels. Kilosort2 models this filtered, whitened data as a sum of spike
646 'templates'. The shape and locations of each template were iteratively refined until the data could be accurately
647 reconstructed from a set of N templates at M spike times. Finally, Kilosort2 output was curated to remove
648 putative double-counted spikes and units with artefactual waveforms. All units not classified as noise were
649 packaged into Neurodata Without Borders (NWB) files (*49*) and analyzed in this paper.

650 PV and SOM cells were identified in their respective mouse lines through a brief opto-tagging session at the end
651 of the recording (*50*). Cells were stimulated with an optical fiber at 40 Hz, 5 Hz, and with a raised cosine

function in 1 s epochs. Blue light was delivered by a 473 nm laser (Laser Quantum, Stockport, United Kingdom) with a measured light power at the tip of the fiber between 12.5-30 mW. The light source was coupled to a 400 µm diameter fiber optic cable (Thorlabs, Newton, NJ), with the tip positioned such that blue light illuminated the entire cranial window. Light was provided using three different types of stimuli, randomly interleaved: 2 ms pulses at 5 Hz, 40 Hz, or a 1s raised cosine ramp. Mice had no exposure to the optotagging stimulus prior to the end of the recording session. Cells whose mean response during the stimulation epoch positively exceeded 2 standard deviations of their baseline prestimulus (100 ms epoch) activity to any of the stimulation types were deemed to belong to the associated interneuron group.

Current source density (CSD) (*51*, *52*) was estimated from the LFP band data by epoching the LFPs, median-filtering with a filter-width of 3 channels, and then downsampling to every 4th channel to retrieve a single vertical/laminar column of responses. CSD was then estimated as the 2nd spatial derivative across multiple contact points according to the equation of (*53*):

$$CSD(t,c) = -\sigma\,(V(t,c-2) - 2V(t,c) + V(t,c+2))/(2s\hat{}2)$$

V(t, c) is the extracellular voltage at time *t* measured at an electrode contact at position *c*, *s* is the inter-contact distance of the electrode array, and σ is the tissue conductivity (here taken as 0.4 S/m). CSD contrasts were computed by grand-averaging the raw LFPs over each condition, then calculating the CSD as above and subtracting across conditions. We corrected for time in task as a confounder via double contrasts**,** first subtracting the 3rd (fully adapted) presentation response from that of the 4th, and then pooling trials within task conditions. These subtractions were treated as normal random variates for a two-tailed, nonparametric spatiotemporal cluster-test that controls the family-wise error rate to $p < 0.05$ to determine significant cross-condition contrasts (*26*). LFP and CSD are smoothed with a width 4 Gaussian filter in both the spatial (laminar) and temporal dimensions for plotting.

<u>Macaque Monkey Experiments at Vanderbilt University: Electrophysiology Experiments</u>

We acquired data using between 1 and 4 linear array multi-channel recording probes. In most experiments, we recorded with 128-channel "deep array" probes where the inter-contact spacing was 25 or 40 µm (Diagnostic Biochips, Glen Burnie, MD) and the coverage was 3.175 mm and 5.08 mm, respectively. In some experiments, we used 32-channel V probes with an inter-contact spacing of 100 µm (Plexon, Dallas, TX) with a coverage of 3.1 mm. We used a mechanical Microdrive (Narishige, Tokyo, Japan) mounted onto the chambers to insert electrodes into the appropriate depth and area. A guide tube was lowered through a recording grid (Crist Instrument Co., Inc.) to penetrate the dura mater and granulation tissue. We then acutely introduced the recording probe into the respective area and waited ~1 hour for the signal to settle before starting the recordings. Recordings were acquired using an RHD System (Intan, Los Angeles, CA) sampling at 30 kHz. Recordings were referenced to the guide tube, which remained in contact with tissue. Grid positions were pre-determined based on a pre-recording MRI scan with the recording chambers and grid in place, with water to mark the trajectories of each grid hole position. We advanced the electrode until there was visually responsive neuronal activity on most channels and until the local field potentials showed a distinct spectral signature of the cortical sheet, characterized by large amplitude alpha/beta (10-30 Hz) oscillations in deep channels and gamma (40-150 Hz) oscillations in superficial channels (*54–58*). Offline, using MATLAB, the data was filtered between 500-

5000 Hz, full-wave rectified, low-pass filtered below 250 Hz, and downsampled to 1000 Hz. We refer to this signal as the MUAe signal, and it reflects the activity of nearby surrounding neurons (*57*, *59–64*).

We allowed three to seven weeks after the optogenetic injections for viral expression before stimulating and recording. Monkey Ca was awake and head-fixed during opto-stimulation. A DBC 128-channel probe with a fiber (an "optrode") attachment (0.2mm in diameter with a numerical aperture of 0.37) at the end was connected to a laser with a wavelength of 473 nm and output power of 318 mW (before fiber). Laser power at the fiber tip was tested in a calibration run with a photodiode at 92.1 mW maximum (SM1-Threaded Mounted Photodiode, Thorlab, Newton, New Jersey) in an Optical Power Monitor (Thorlab, Newton, New Jersey). On recording days, the optrode was advanced into the injection site (in MT, MST, 8a, and PFC in separate sessions) with a metal guide tube puncturing the dura mater. Electrophysiological signals were recorded on the same optrode and a non-optrode neural probe simultaneously in another area. For analysis of the monkey optogenetics dataset, we used isolated single units and used the same spike sorting techniques that were applied to mouse data (Kilosort2).

Neurons were stimulated with a 5 Hz and 40 Hz raised cosine function at 3V, 4V, 5V amplitudes, at maximum output power of 13.9 mW, 71.2 mW, and 92.1 mW, respectively. Instantaneous firing rate was estimated by smoothing binary spike trains, using a nonparametric EPSP filter (20ms smoothing window). Mean spike waveforms, attributes (trough-peak duration, voltage distribution along the probe), and quality metrics (presence ratio, overall firing rate, signal-to-noise-ratio, and inter-spike interval violations) were manually checked for each Kilosort2 sorted optotagged unit, and noisy/artifactual units based on these attributes were removed prior to analysis. Each single unit's firing rate during laser stimulation (2000 ms) was compared with baseline (1000 ms before onset and 1000 ms after offset). Trial-averaged mean firing rates for each laser frequency and power level were compared with baseline using one-tailed Wilcoxon signed-rank tests ($\alpha = 0.05$, right-tailed). Magnitude-squared coherence between the laser and each unit was computed across the spectrum of all laser stimulation frequencies. Coherence was defined as significant under two criteria: if coherence of spiking and laser during laser interval was higher than for spiking during the pre- and post-baseline, and if coherence surpassed a critical value (*65*). Units significant for increased firing rate and coherence were considered optotagged.

<u>Mouse Experiments at the Allen Institute: Visual Stimulation Parameters</u>

All Neuropixels recordings were according to the standardized Neuropixels visual coding pipeline. Visual stimuli were generated using custom PsychoPy scripts and displayed using an ASUS PA248Q LCD monitor with 1920 × 1200 pixels (55.7 cm wide, 60 Hz refresh rate). Stimuli were presented monocularly, and the monitor was positioned 15 cm from the right eye of the mouse and spanned 120 dva × 95 dva. Monitor placement was standardized across rigs such that the mouse's right eye gaze would typically be directed at the center of the monitor. Then, a sequence of drifting gratings appeared (full-screen, 4 Hz drift rate, 1 cycle/degree, 0.8 Michelson contrast, angle of the drifting grating was 45 or 135 degrees from the vertical midline) for 500 ms, and was replaced by a blank screen with the fixation dot remaining for 500 ms. This sequence was repeated 4 times in a trial, for a total trial length of 4500 ms (500 ms pre-sequence fixation + 4 x 1000 ms stimulus presentations). Every 100 sequences, a period of a blank, black screen was presented for 10 s.

Macaque Monkey Experiments at Vanderbilt University: Visual Stimulation Parameters

We used MonkeyLogic (developed and maintained at the National Institute for Mental Health) to control the behavioral task (*66*). Visual stimuli were displayed using PROPixx Pro projectors (VPixx Technologies, Quebec, Canada) with a resolution of 1920 x 1080 at a 120 Hz refresh rate. The projector screen was positioned 57 cm in front of the monkey's eyes. Luminance calibration was performed with a Photo Research PR-650 at the projector screen with a median value of 2.613 cd/m^2.

The monkey was trained to fixate its eyes around a central fixation dot (radius of fixation window: 1.5 dva). Eye position and pupil diameter were monitored using an Eyelink 1000 (SR Research, Ottawa, Canada) at 250 or 500 Hz. A task began with an isoluminant gray screen. Once the monkey maintained fixation for 500ms, a sequence of drifting gratings appeared (12 visual degree radius, 2 Hz drift rate, 1 cycle/degree, 0.8 Michelson contrast, angle of the drifting grating was 45 or 135 degrees from the vertical midline) for 500 ms, and was replaced by a blank screen with the fixation dot remaining for 500 ms. This sequence was repeated 4 times in a trial, for a total trial length of 4500 ms (500 ms pre-sequence fixation + 4 x 1000 ms stimulus presentations). The monkey was rewarded with a small juice reward for maintaining fixation throughout the trial.

Mouse Experiments at the Allen Institute: Habituation to Predicted Sequence

Mice were habituated over the course of 5 behavior-only sessions in which only the predicted sequence (either x-x-x-y or y-y-y-x) was presented. This resulted in 2000 habituation trials before recordings.

Macaque Monkey Experiments at Vanderbilt University: Habituation to Predicted Sequence

Monkeys were habituated to a predicted sequence over the course of 3 behavior-only sessions in which only the predicted sequence (either x-x-x-y or y-y-y-X) was presented. This resulted in 2850 complete habituation trials before recording sessions. Subsequently, after a recording session, monkeys were again re-habituated to one of the predicted sequences before the next recording session.

Mouse Experiments at the Allen Institute: Data Analysis

We recorded 29977 total putative single units, averaging 359 (+/-42) units per animal and 60 (+/-3) units per probe. We further restricted the units for analysis, consistent with previous reports using the same methods for analyses (*23*), to those that exhibit a visual response that exceeded 5 standard deviations of the baseline firing rate, minimum of 0.1 sp/s, inter-spike interval (ISI) violations below 0.33, a presence ratio above 0.95, an amplitude cutoff below 0.1, and were found to be in areas V1, LM, RL, AL, PM, AM, or LP. This resulted in a sample of 5389 units from 15 of 16 mice. No units from 1 mouse passed the criteria due to a destabilizing event during the recording. Additionally, data from another mouse were omitted from the analysis due to issues with the visual stimulus timing. As a result, our final sample consisted of 5062 single units from 14 mice.

Macaque Monkey Experiments at Vanderbilt University: Data Analysis

We recorded a total of 6,619 sites with MUAe signals across 8 cortical areas across 19 recording sessions: 640 in PFC, 416 in FEF, 512 in MST, 512 in MT, 1056 in V4, 1536 in V3, 896 in V2, and 1024 in V1. These MUAe signals were extracted from broadband signals with a Butterworth filter of stopbands at 450 Hz and

5500 Hz and passbands at 500 Hz and 5000 Hz. For analysis, we restricted these sites that had visually evoked activity, which was determined by whether the period from 50-250 ms post-stimulus was significantly greater than pre-stimulus baseline (using a threshold of $p<0.05$, rank sum test). The resulting population used for analysis consisted of 508 sites in PFC, 177 in FEF, 161 in MST, 252 in MT, 230 in V4, 569 in V3, 328 in V2, and 270 in V1.

Macaque Monkey Experiments at Vanderbilt University: Laminar Identification

For each penetration of monkey recordings, we examined its trajectory based on the MRI image and postmortem Nissl staining images. Penetrations that are not sufficiently perpendicular to cortical layers or did not have enough cortical coverage were excluded from layer-based analyses. We then examined the multi-unit activity, CSD, and spectrolaminar pattern (*55*) across depth for each penetration. Layer 4 of each area was identified based on the best corresponding electrode location with the earliest MUA onset, earliest CSD sink, and spectrolaminar high/low band relative power crossing. Total area thickness was measured in MRI images of each monkey for each area. We also obtained percent thickness per layer for each area from existing data (*67*). The number of electrodes per layer was then calculated by multiplying the total layer thickness by the thickness of each layer for each area. We then assigned the layer position of each electrode by counting from the previously identified layer 4 electrode up to layer 1 and down to layer 6.

Granger causality analysis

In mice, we began by defining all available single units in each area. We took all cortical neurons for this analysis, and per mouse and probe, included an area in the analysis if a minimum of 12 single neurons were simultaneously acquired. This resulted in six neuronal spiking time series, one per area. Granger causality was calculated separately per mouse and for local and global oddball trials, using all available trials. We calculated Granger causality using a non-parametric implementation (*29*, *30*). For this, we computed Fourier coefficients using the Fieldtrip toolbox (*68*) using a sliding window approach, utilizing 200 ms time windows for analysis. We computed the Fourier coefficients using multitapers (3 multitapers per trial, time window size = 200 ms, smoothing = 10 Hz, function ‘ft_freqanalysis’, using method ‘mtmfft’, frequencies 0-100 Hz were calculated). One time window was on the baseline, from 100 ms pre- and 100 ms post-oddball onset. Two time windows reflecting stimulus processing were also used, one centered from 100 ms to 300 ms post-oddball onset, another from 300 ms to 500 ms post-oddball onset. Bivariate Granger causality was computed pair-wise between all available neuronal spiking time series (using ft_connectivity analysis with method = ‘granger’ and granger.sfmethod = ‘bivariate’).

Statistics and Visualization

In mice, spiking activity for each cell was normalized by their average activity level to produce an arbitrary value that was less variable across units with differing firing rates. In monkeys, spiking activity for each channel was normalized to each channel’s standard error across trials. Unless otherwise noted, all statistics were performed using nonparametric, cluster-based permutation testing (*26*) of the spiking activity at either the single-(multi)unit level or the population level, with alpha thresholds set to 0.05 for both test stages. We also required that a statistically significant difference persist for at least 25 ms as indicated by this test. Data was

smoothed with a 50-ms moving mean window. Confidence bands, where displayed, are computed for a 95% confidence interval across units' condition-wise mean activity included in the population.

Feature selectivity was measured the same way as in a previous report (*17*). First, we determined the mean response to each stimulus during visual stimulation (0-500 ms following stimulus appearance) and during a separate presentation block where stimulus order was randomized. For each unit, we subtracted the mean response to the GO-orientation stimulus from the LO-orientation stimulus and divided it by the sum of those two means. Single units with this index above 0.8 or below -0.8 were defined as highly selective for the GO orientation or the LO orientation, respectively.

For identifying the onset latencies of significance, a t-test was run at each time point during 500ms of stimulus presentation for individual unit/channel (with the same selection criteria described above, only including unit/channel with significant visually evoked activity), and the first contiguous significant cluster larger than 10ms was considered the onset of significance for that channel.

Data and Code Availability

All mouse data used in this work are openly available through the DANDI Archive (dandiset id: 000253, doi: https://doi.org/10.48324/dandi.000253/0.240503.0152). Software resources for the analysis of this dataset are provided here: https://alleninstitute.github.io/openscope_databook/projects/glo.html. The code to generate the global-local oddball sequences is provided here: https://github.com/AllenInstitute/openscope-glo-stim.

Supplementary Text

Neuronal Selectivity analysis for local and global oddball processing (in mice)

The increased response observed during local oddballs (Fig. 2) cannot be explained by the fact that the oddball is a different stimulus (compared to the rest of the stimulus sequence) since we averaged across all neurons (thus eliminating any tuning-based preferences for one or the other stimulus) and about half of the animals saw the orthogonal orientation as the oddball stimulus. Moreover, across all recorded single units in the dataset, we found a highly similar number of units strongly preferring each of the two orientations (LO-orientation: 21.2% of all single units, GO-orientation: 22.3% of all single units). This indicates that there was not a strong response bias for one oddball feature over the other within the population of measured units. To summarize, even after completely randomizing neuronal biases, the local oddball stimulus consistently evoked a larger response when we examined spiking activity across layers, areas, and animals.

Previous reports have suggested that sensory prediction error signaling might be isolated to neuronal populations that are selective for the features that define the error-producing stimulus (*17*). To test for this possibility, we isolated the population of GO-orientation selective neurons within our recorded populations and determined whether they specifically harbored a global oddball detection signal. Of the 22.3% of single units strongly selective for the GO orientation (relative to the LO orientation), only 6.1% were also significant GO detectors. This is comparable to the rate of GO detectors we observed in the general population (6.4% of single units). In other words, GO detection was not isolated from featuring selective populations, nor were all units highly selective for the GO stimulus found to be GO detectors.

Additional Details on Granger causality analysis

We calculated Granger causality (GC, see Methods) to quantify directed functional connectivity amongst neurons and address the directed propagation of oddball responses throughout the hierarchy. For each cortical area and mouse, we combined all available single neurons to create a population spiking time series (a minimum of N=12 neurons per area were used to create this population spiking time series). We then calculated GC between each pair of cortical regions, using the anatomical hierarchical ordering: V1, RL, LM, AL, PM, AM (in order from the earliest to the latest area in the mouse visual hierarchy (*69*)). This generated 30 inter-areal GC values, one for each area pair and direction of influence. We computed the GC hierarchical asymmetry for each pair of areas by subtracting the feedforward GC from the feedback GC. For example, the feedforward GC from V1 to RL was subtracted from the feedback GC from RL to V1. A positive difference indicates that feedforward GC > feedback GC. A positive difference for global oddballs would be consistent with the hypothesized (H1, Fig. 1A) feedforward propagation of prediction error. We compared oddball GC responses during stimulus processing in both the early (100-300 ms post-oddball onset) and late (300-500 ms post-oddball onset) time windows between local and global oddballs. We compared them to baseline (100 ms pre- and 100 ms post-oddball onset). GC became significantly hierarchically asymmetric in the feedforward direction for local, but not global, oddballs during both early and late periods (Fig. 4B-D, Wilcoxon rank sum test of GC hierarchical asymmetry values across mice vs. pre-oddball baseline, $P<0.01$). In contrast, GC hierarchical asymmetry did not change during global oddballs compared to baseline (Fig. 4B-D, Wilcoxon rank sum test of GC hierarchical asymmetry values across mice vs. pre-oddball baseline, all comparisons, $P>0.01$).

Current Source Density analysis

To determine whether top-down prediction signatures might be latent in synaptic dynamics rather than spiking activity, we examined the Current Source Density (CSD, a measure of local net depolarization) profiles during global oddball detection in mice. CSD is frequently used as a proxy for synaptic activity occurring along the cortical column (*54*, *58*, *60*, *63*, *70–81*), which reliably reflects columnar processing dynamics, including those that may be missed by spiking activity (*56*, *57*, *82*). We computed CSD from the local field potential responses to the GLO and control sequences (Fig. S4) and then performed the same global oddball contrast as with the spiking data. We hypothesized that a difference in current sinks in the upper or deep layers of the cortex might manifest during prediction errors (i.e., when the global oddball stimulus unpredicted in the main experimental block as compared to the control block). During global oddballs, we did not observe reliable changes in synaptic activation at the earliest stage of visual cortical processing (i.e., in V1, Fig. S4B), neither before nor after visual stimulation. Specifically, we did not observe significant, reliable synaptic changes in the extragranular compartments, which would indicate top-down influences in deploying a prediction to earlier areas. We observed the same in downstream visual cortical regions (Fig. S4C). This shows the predictions are not being deployed widely through synaptic modulations.

Neural Instantiation of Predictive Coding

Predictive coding theorizes an internal model of the environment's statistics; these statistics are typically taken to include the mean expected stimulus (typically denoted mathematically as μ) and the precision of the predicted stimulus (typically denoted mathematically as Π). In other words, PC is both subtractive and multiplicative: when sensory signals do not match the prediction, subtraction results in a larger value, called the prediction error, which is weighted by precision (Fig. 1). This error signal has been proposed to be computed in

superficial layers 2 and 3 of the sensory cortex, which propagate the signal in the feedforward direction up the cortical hierarchy (*2*, *7*, *11*). As a second-order statistic, the precision Π is always a positive, nonzero quantity, ensuring that prediction errors are fed up with the cortical hierarchy, even if attenuated. As they ascend, prediction errors instigate updates to the internal model to improve predictions, and associated prediction update signals flow back down the hierarchy.

On Hierarchical Predictive Coding

PC has also been proposed to occur over a series of computational steps, each comparing predictions to prediction errors from a previous step (*3*). This "hierarchical predictive coding model" has since been modified to fit the neocortex's structural and functional architecture (*2*, *12*) (Fig. 1A). These hierarchical models efficiently predict and explain the cortical responses to first-order pattern violations ("local oddballs"), such as a change from repeated stimulation (e.g., a stimulus sequence such as x-x-x-y) (*19–21*). Such local oddball responses depend on a simplified predictive model that the current stimulus will continue to repeat. However, local oddball responses persist during states of deep anesthesia when feedback connections are functionally weak (*16*, *83*). As such, they do not provide strong evidence for PC, which envisions rich and multi-faceted predictions feeding back and modulating early sensory processing (*2*, *4*, *11*, *84*). It is an open question whether more complex prediction errors engage the sensory cortex (*15*, *20*). More complex prediction error computations and higher-order predictions can be studied using "global oddballs." These second-order pattern violations occur when a repeated presentation of first-order pattern violations is interrupted (e.g., x-x-x-y / x-x-x-y / x-x-x-y / x-x-x-x). Global oddballs are a repeated stimulus, so responses cannot be explained by recent stimulus history, i.e., release from adaptation. As of now, there is only indirect evidence from human and non-human primate studies using functional Magnetic Resonance Imaging (fMRI), magneto- and electroencephalography (M/EEG), and local field potential (LFP) for global oddball responses in the sensory cortex (*20*).

Experimental Design Notes and Rationale

Two cohorts of mice, each habituated to a different stimulus sequence, participated (Fig. S1A). To counterbalance the stimulus set across the population of animals, one cohort was habituated to a sequence of 3 rightward oriented gratings followed by a leftward-oriented grating (x-x-x-y, we refer to each stimulus in order as P1, P2, P3, P4), the other cohort to 3 leftward then a rightward (y-y-y-x). Following a 500 ms baseline, each stimulus was presented for 500 ms (with a 500 ms interstimulus interval) for a total trial duration of 4500 ms . Mice were habituated to these sequences (n=8 mice for x-x-x-y and n=8 mice for y-y-y-x sequences) throughout five sessions totaling 2000 trials. Two macaques were habituated to these sequences with the additional requirement of central fixation of the eyes on the screen. Monkeys were habituated over three sessions for 2850 complete trials before recordings. Then, in the experimental session, mice/monkeys were exposed to the not-yet-experienced global oddball sequence with a lesser frequency (20%). After that main experimental block, mice/monkeys experienced a block of random orientation sequences ("Random" block) before the "Control" block, where animals viewed alternating x-x-x-x and y-y-y-y sequences, rendering the same stimuli used in global oddball trials predictable. These controls were included to evaluate oddball detection in conjunction with the responses in the GLO experimental block.

Pupil response differences between species

Note that although mice responded to oddballs with enhanced pupil dilation (Fig. S2A), monkeys responded to oddballs with enhanced pupil constriction (Fig. S2B). This difference could have been due to either a species difference or due to differences in how visual stimulation was delivered - namely, mice were headfixed on a trackball, stimuli were delivered to the right eye, and were not required to fixate. Monkeys were headfixed and required to fixate on a central point of the screen throughout the trial. These results are congruent with previous work. Under similar conditions, previous studies have shown that monkey pupils constrict to visual stimulation onset (*85*) and mouse pupils can either constrict or dilate, depending on the deviance of the stimuli (*86*).

Additional Considerations

While our findings are inconsistent with the hypothesized ubiquitous elements of Predictive Coding, additional issues should be considered. For one, we have chosen to study pure global oddballs, deviations from predictions induced by the lack of a stimulus change. Other forms of prediction that depend on local stimulus change (e.g., a stimulus that is both a local and global oddball) have been found in the mouse visual cortex in other experiments (*17*, *18*, *23*). However, more complex forms of prediction processing envisioned by PC models, such as the global oddball and omission responses (*84*, *87*, *88*), do not appear to engage visual sensory cortical responses with stimulus-specific activity (*89*), as we have found.

Another important consideration is the degree of attention paid to the oddballs by the animals. Previous work suggested that global oddballs are not observed under certain states of unconsciousness (*16*, *83*). Given the close relationship between conscious awareness and attention (*90*), attention may be a prerequisite for global oddball processing (*21*). However, given the pupillary responses of the animals in these experiments (Fig. S2), it is likely that the animals recognized the oddball stimuli (both local and global) as oddballs, and that some amount of attention was paid to the oddballs. In addition, the finding that local oddballs evoked reliable activity in ~50% of neurons suggests sufficient attention was paid to the stimulus sequences. Finally, global oddballs were observed in monkeys' prefrontal areas and higher-visual regions of mice and monkeys. Thus, despite being available to the animals' higher cortex and evident in behavior as measured by pupil responses, they did not profoundly affect sensory responses.

Also, hierarchical predictive coding models have postulated that prediction error signals are modulated by a gain term that takes on a functional interpretation in terms of precision (Π in Fig. 1A, see also (*91*)). That being said, models that consider gain in terms of precision require that precision be positive and nonzero (*92*), entailing that prediction error signals might be attenuated but never entirely quashed by gain modulation. Future studies should explicitly consider the role of gain modulation on prediction error responses by manipulating the attentional state.

945 **Fig. S1-S11**

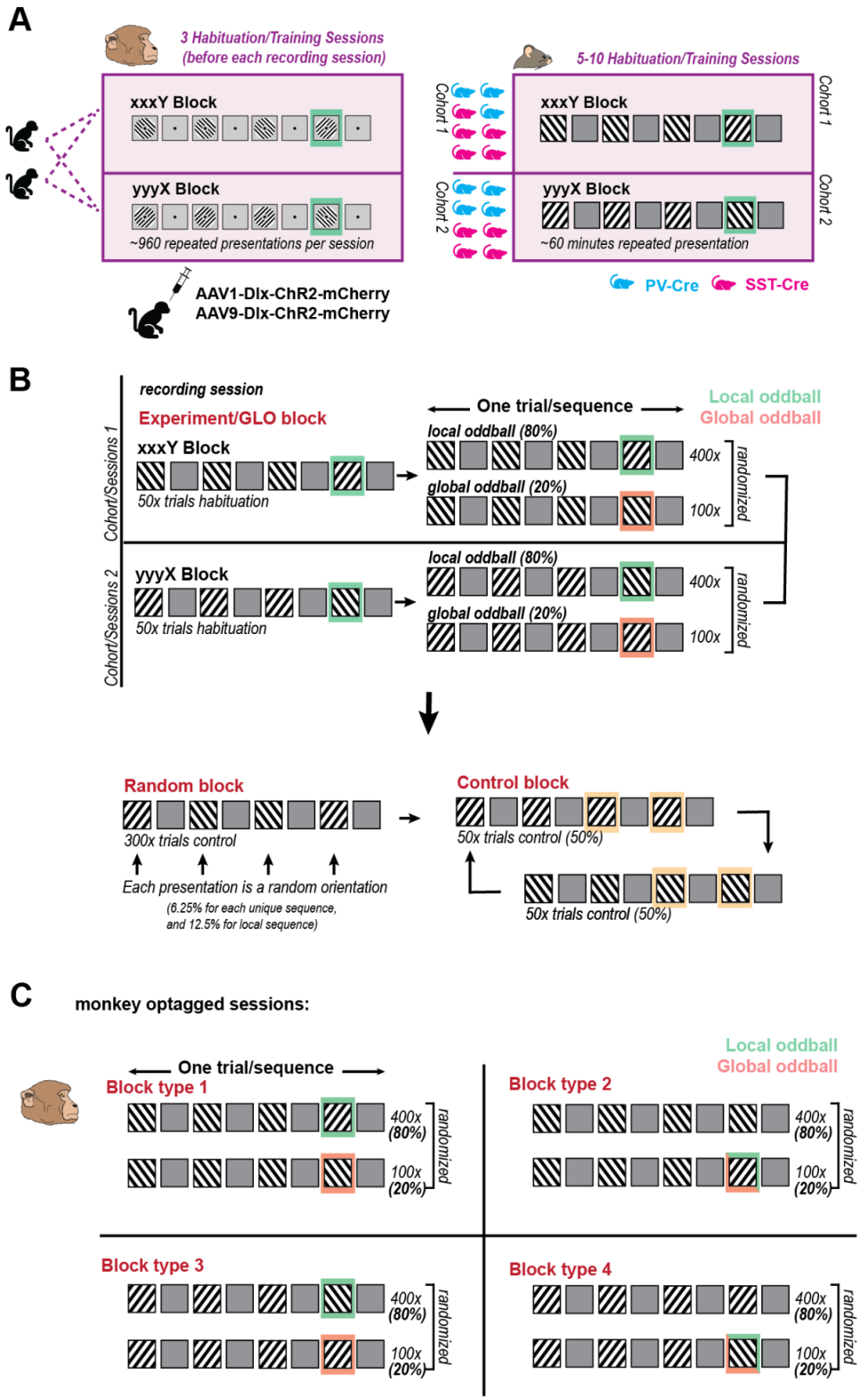

946 **Fig. S1 Experimental Design.** (A) 2 macaque monkeys were habituated to the local oddball pattern (x-x-x-y or y-y-y-X on a given

recording week) for ~960 repeated presentations for 3 days prior to recording day. 16 transgenic mice were used in the experiment; genotypes were selected to allow for optotagging of either somatostatin- (magenta) or parvalbumin-positive (cyan) interneurons. Mice were split into 2 training groups: 1 group exposed to x-x-x-y sequences during the entirety of training and 1 group to y-y-y-X. (B) Recording sessions were divided into 3 blocks. In the experiment (GLO) block, animals experienced their trained 'Local' oddball sequence (x-x-x-y or y-y-y-X) for a 50-trial habituation period. Then, on 20% of the next ~500 sequences, they observed a never previously seen 'Global' oddball sequence (x-x-x-x or y-y-y-y). A block of random sequences of 4 stimuli followed the experiment block (resulting in a 6.25% probability for each unique sequence, with the sequence identical to the local oddball sequence upsampled to 12.5%). A control block followed where sequences of x-x-x-x (50%) and y-y-y-y (50%) were experienced. (C) Opto-tagging sessions in monkeys were performed with a classical local/global oddball paradigm to ensure cell stability between oddball and control trials.

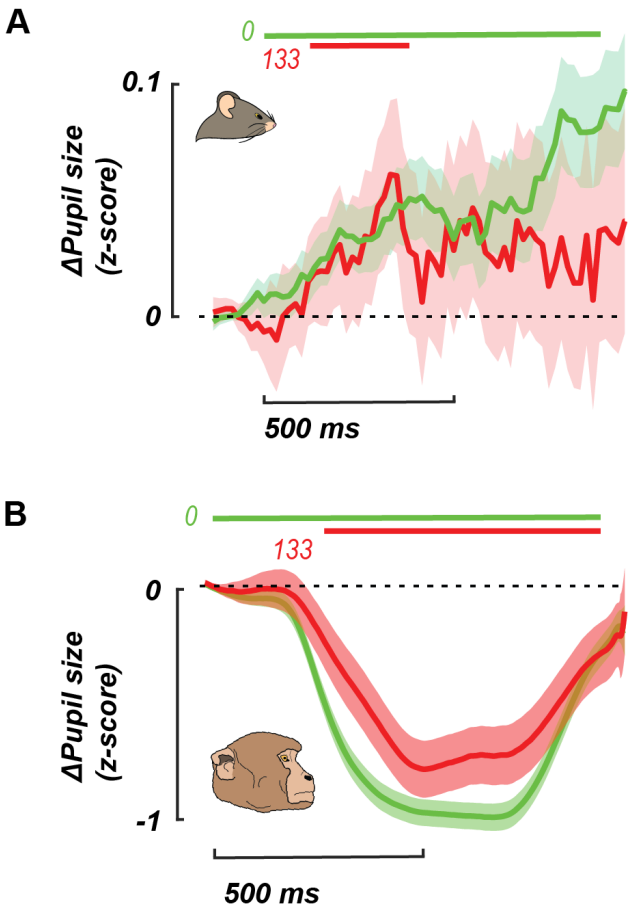

Fig. S2 Global oddball detection indicated by pupillary response. (A) Green trace shows average z-scored change in pupil size between P4 (oddball) vs. P3 (stimulus prior to oddball) during a local oddball sequence. Red trace shows average z-scored change in pupil size between P4 (oddball) vs. P3 (stimulus prior to oddball) during a global oddball sequence. Colored bands represent 95% confidence interval. (B) Same as panel A, in monkeys.

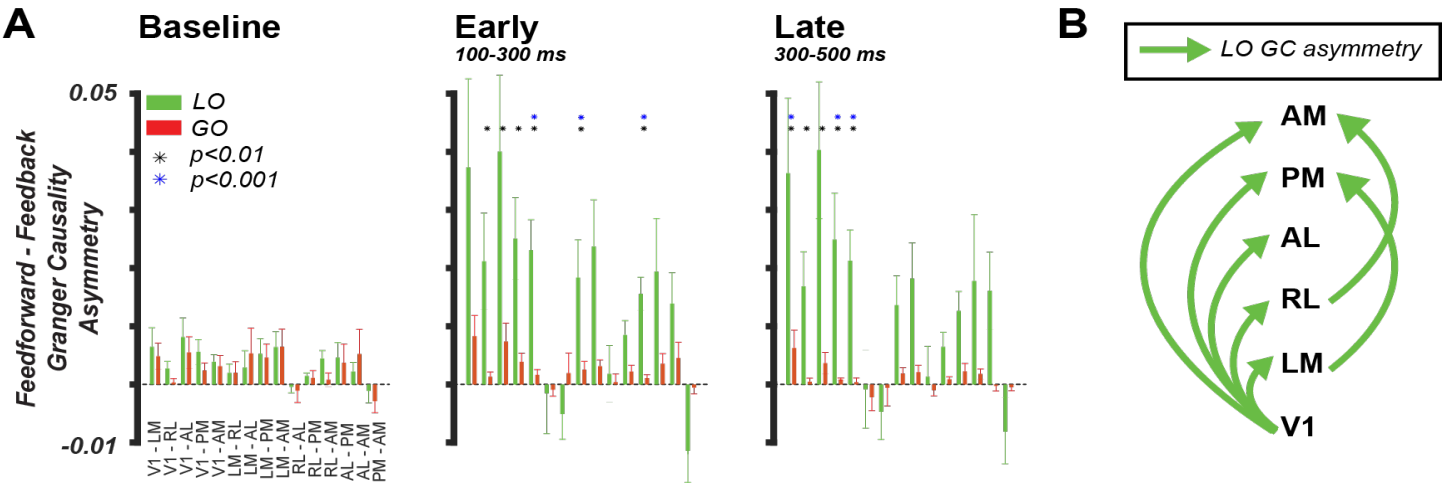

Fig. S3 Cortical spiking causalogram for local and global oddballs: Granger causality as a function of time across brain areas. (A) Granger causality asymmetry (Feedforward minus feedback GC) between all possible areas in the baseline (left, pre-oddball time window; middle, initial sensory processing period; right, late sensory processing period). Green bars denote local oddballs, and red bars denote global oddballs. Mean across mice, + or - SEM across mice. Asterisks indicate connections that are significantly different from the baseline at P<0.01 (black asterisks) and at P<0.001 (blue asterisks). (B) Hierarchical summary of significant changes in GC asymmetry from pre-oddball baseline for local oddballs. Significant interactions at P<0.01 and P<0.001 are shown, and both early and late periods are depicted. Global oddballs are not shown because no significant changes in GC asymmetry were observed.

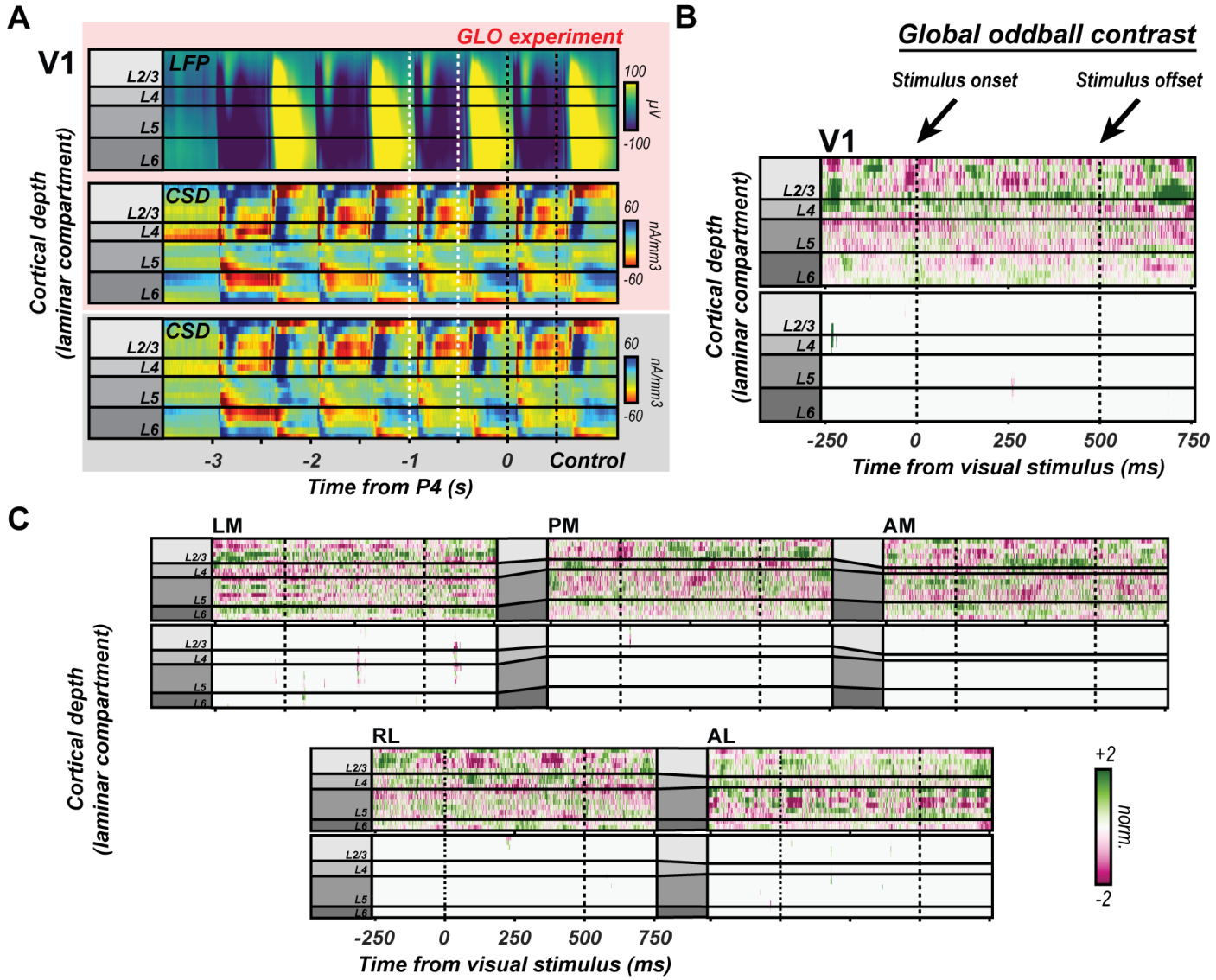

Fig. S4 CSD reflecting synaptic activity does not indicate top-down predictions being fed back to the early sensory cortex. (A) Laminar CSD is calculated from the LFP response (top) to sequence presentations averaged across trials and mice (n=9) for area V1 after aligning cortical depth between animals. CSD is calculated for the global oddball experimental condition (middle, red highlighted region) and control condition (bottom, gray highlighted region). The epoch between the white dotted lines indicates presentation 3, and between the black dotted lines indicates the global oddball presentation (middle) or presentation 4 in the control (bottom). (B) Evaluating the global oddball contrast for evidence of differences in synaptic activity with global oddball detection in V1. Difference of differences identical to previous global oddball contrasts (P4-P3) for the CSD data. The top image indicates all values following the contrast and normalization between -2 and +2 standard deviations. The bottom image shows the same data with a mask applied to display only significant values (Welch's t-test, $p<0.01$). Color map intensity is indicated by the scale bar at the bottom right of the figure. (C) Difference of differences for global oddball contrast for the remaining visual cortical areas. Formatting identical to B.

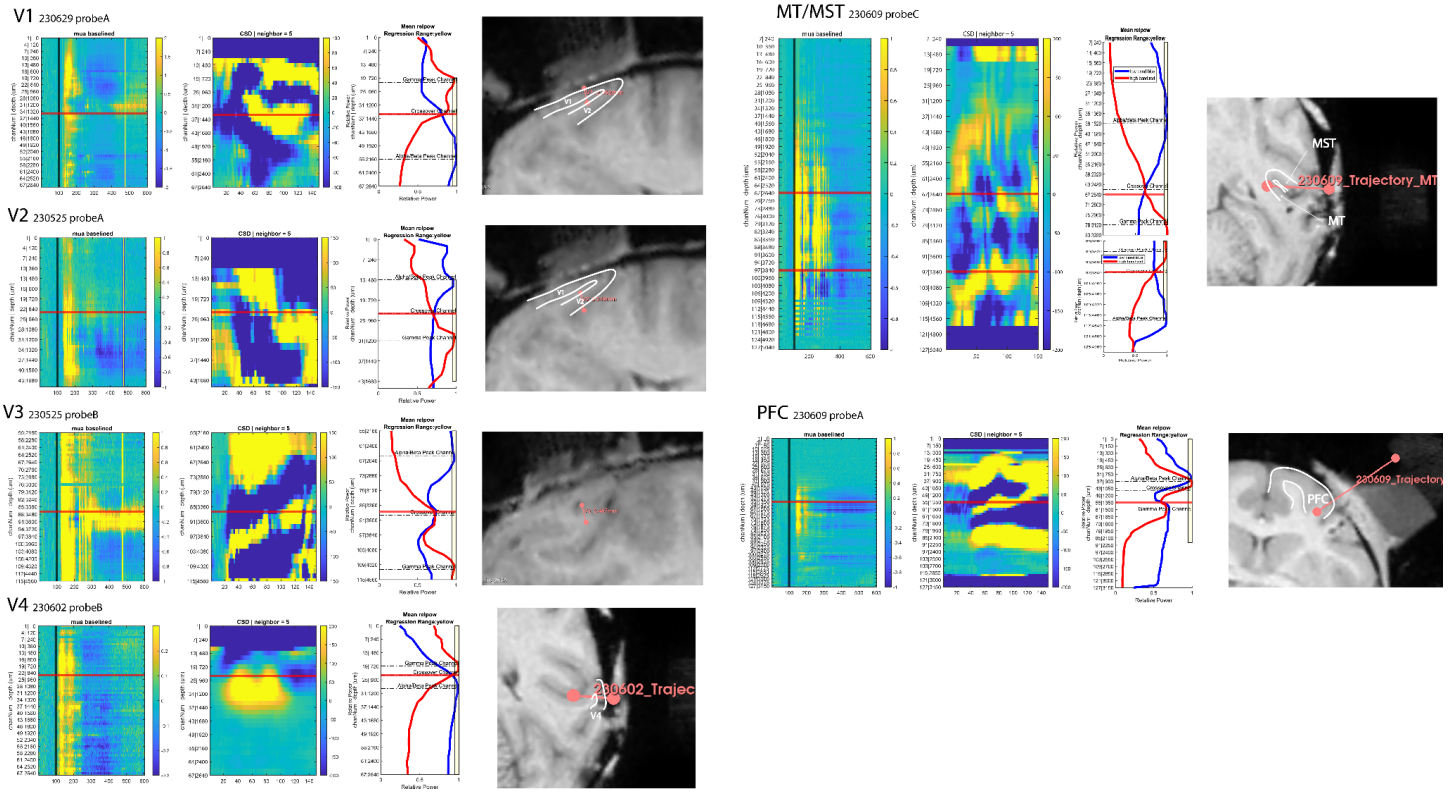

Fig. S5 Spectrolaminar profile of monkey electrophysiology recordings included in layer-specific analyses. Panels for each area, from left to right, show corresponding evidence for layer 4 identification using the earliest onset of MUA channel, earliest sink in current source density, beta/gamma relative power crossing, and MRI anatomical reconstruction of the corresponding electrode trajectory.

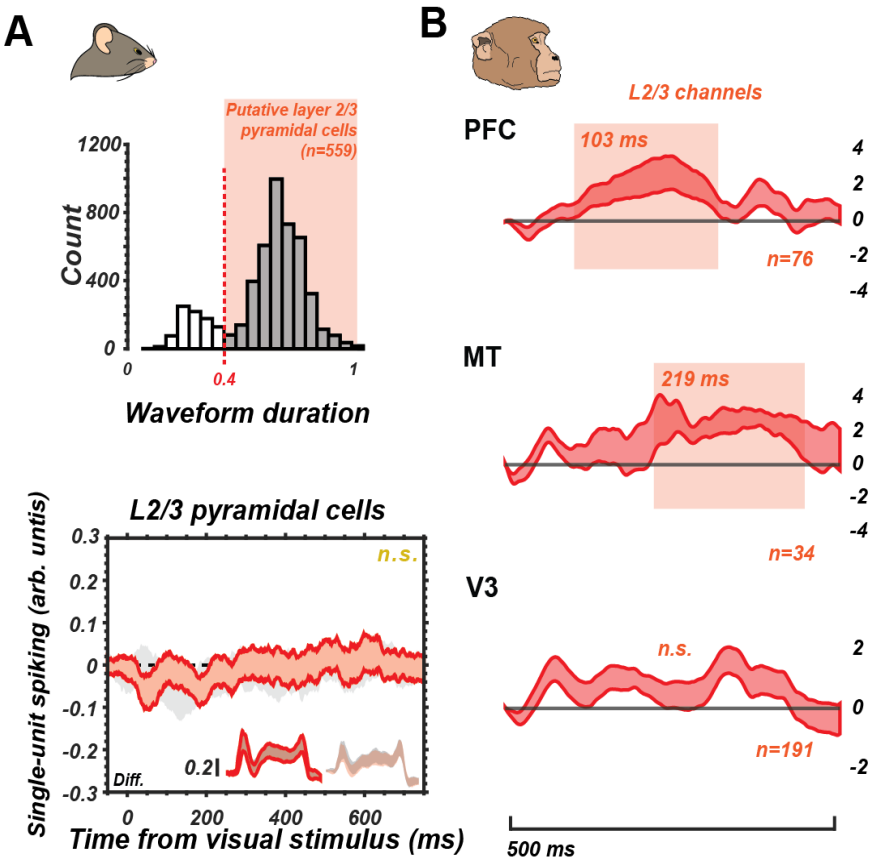

Fig. S6 Putative layer 2/3 neurons do not harbor latent feedforward global oddball signals. (A) Global oddball response in putative layer 2/3 pyramidal cells in mice. To identify layer 2/3 pyramidal units in mice, we eliminated single units that were found to be inhibitory interneurons via optotagging, we eliminated units found outside layer 2 or 3, and we ensured units that had a spike waveform duration of longer than 0.4 ms (waveform duration histogram is shown in upper subplot), which primarily reflects broad-spiking pyramidal cells (*32*). (lower subplot) Red bands are P4-P3 in the main block; gray bands are P4-P3 in the control block. Insets show raw traces of P4 and P3 presentation responses. (B) Global oddball responses in L2/3 in monkeys in areas that had population significant global oddball responses (V3, MT, PFC) and in which laminar recordings were possible. Red bands are P4-P3 in the main block for global oddball trials compared to the control block, time-locked to oddball onset. Mean +/- 2 SEM (N indicates number of channels). Shading indicates significant clusters of significance in time. Numbers within shaded region indicate the onset of the cluster in ms.

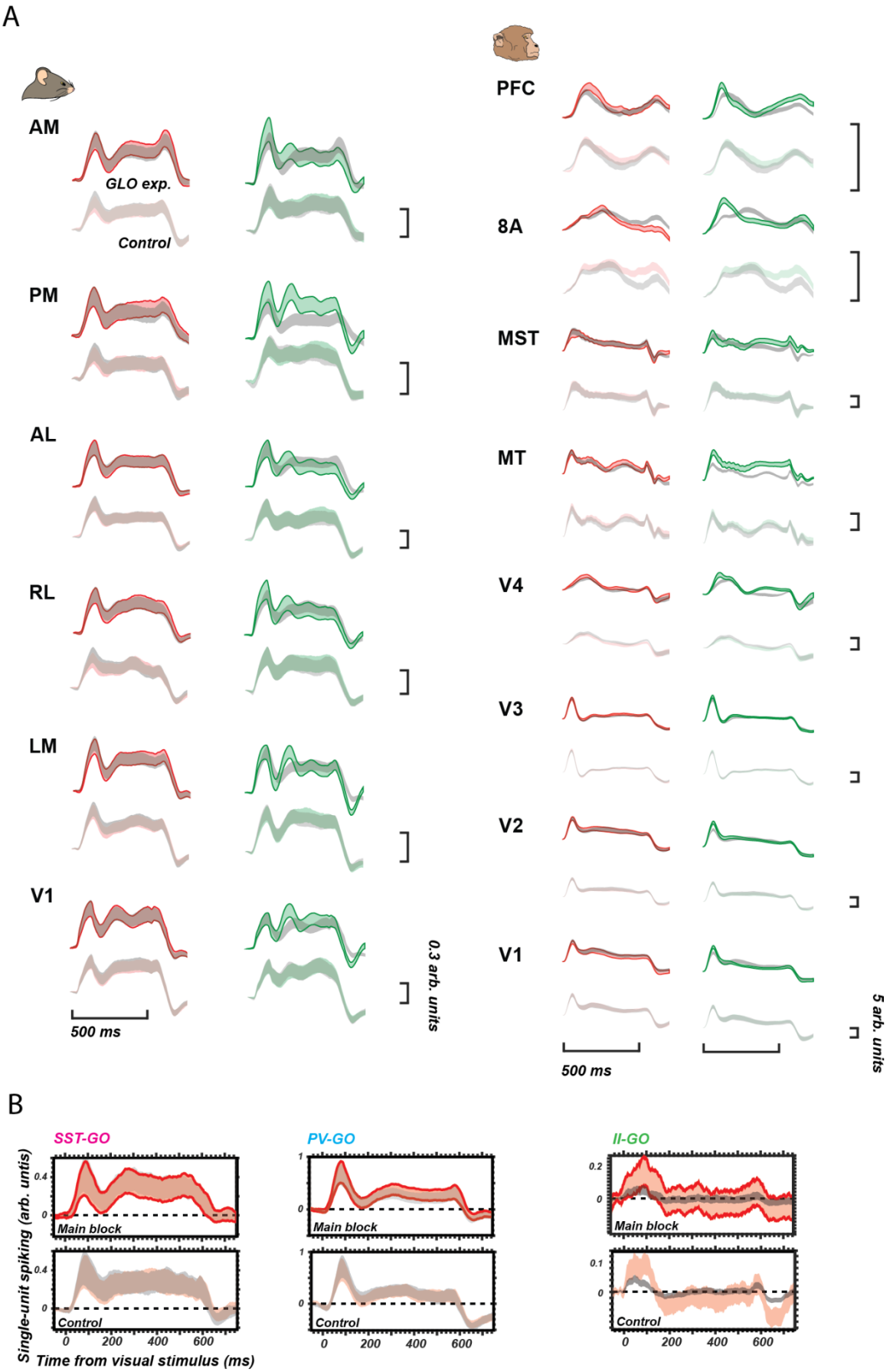
A
AM
GLO exp.
Control
PM
AL
RL
LM
V1
500 ms
0.3 arb. units
PFC
8A
MST
MT
V4
V3
V2
V1
500 ms
5 arb. units
B
SST-GO
PV-GO
II-GO
Main block
Control
Single-unit spiking (arb. untis)
Time from visual stimulus (ms)

Fig. S7 Component traces of global and local oddball contrast. (A) For each area, red and green outlined traces (top) show 95% confidence interval of P4 of global oddball (left, red) and local oddball (right, green), and overlapping grey traces show 95% confidence interval of P2 of the same sequence. Red and green non-outlined (bottom) show 95% confidence interval of P4 of control sequence, and overlapping grey traces show 95% confidence interval of P3 of the same sequence. The green traces shown the corresponding local oddball responses. (B) single unit normalized spiking responses in optotagged inhibitory interneurons (left panel, SST cells in mice; middle panel, PV cells in mice; right panel, inhibitory interneurons in monkeys, Bands are 95% confidence intervals across units. Top, main block spiking response with red P4 and gray P3. Bottom, control block spiking response with red P4 and gray P3.

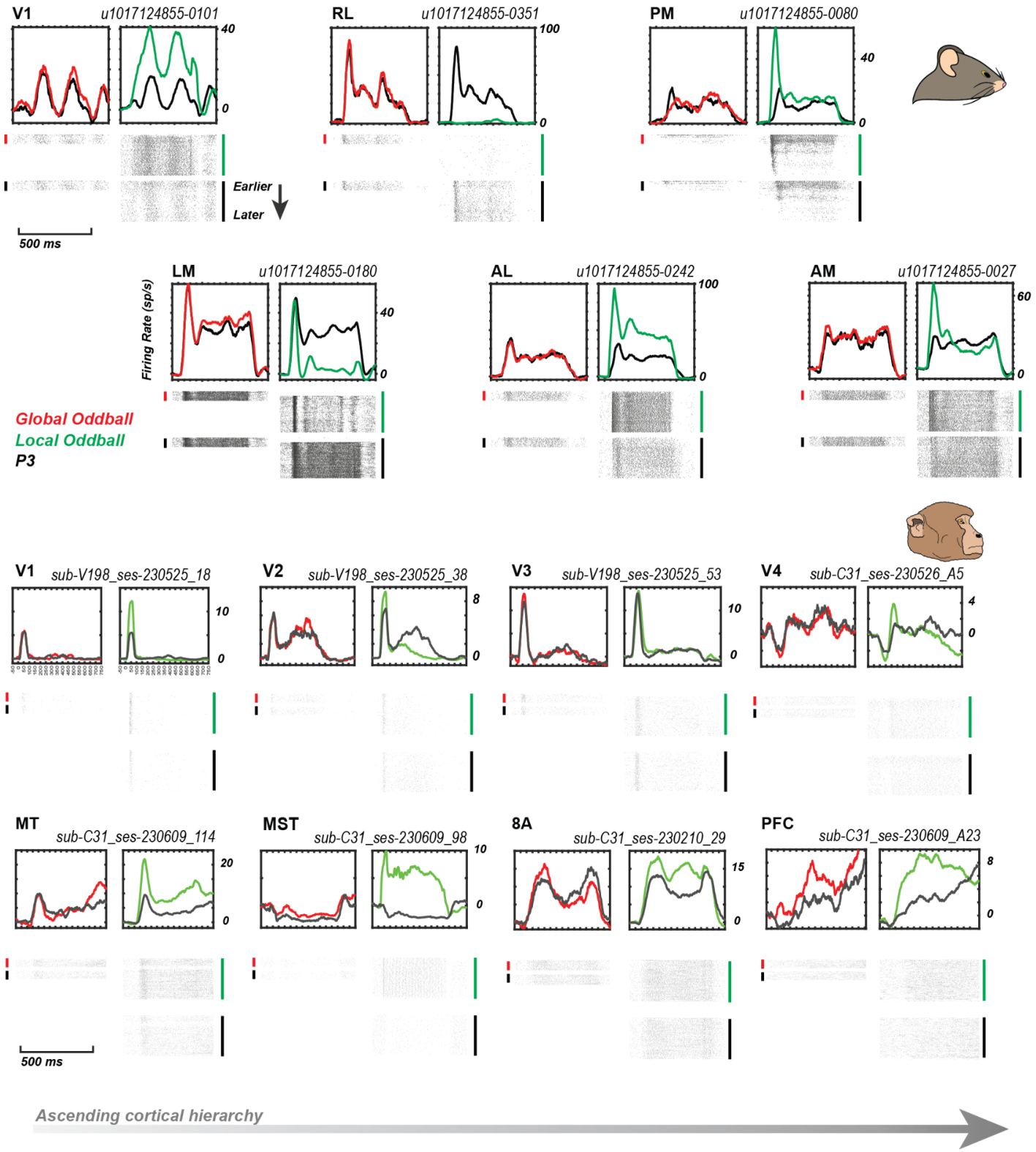

Fig. S8 Examples single-unit responses in mice and monkeys. For each area in the mouse and monkey, one example single-unit is displayed. For the mouse areas, all single-units come from one mouse (1017124855). For the monkey, units are taken from two monkeys (V198, C31). The top left subpanel of each unit displays the convolved spike train for the P4 global oddball response (red) and the local oddball response (green) on the right. The respective P3 responses (black) immediately prior to each oddball type are displayed on the same axes. Below the convolutions are the raster plots for each condition. Top left, global oddball; bottom left, P3 on

global oddball sequences; top right, local oddball; bottom right, P3 on local oddball sequences. Topmost line in each raster is the first trial of each condition with the subsequent lines being later in the session. There are fewer rasters for the leftside plots as global oddball occurred in only 1 in 5 trials.

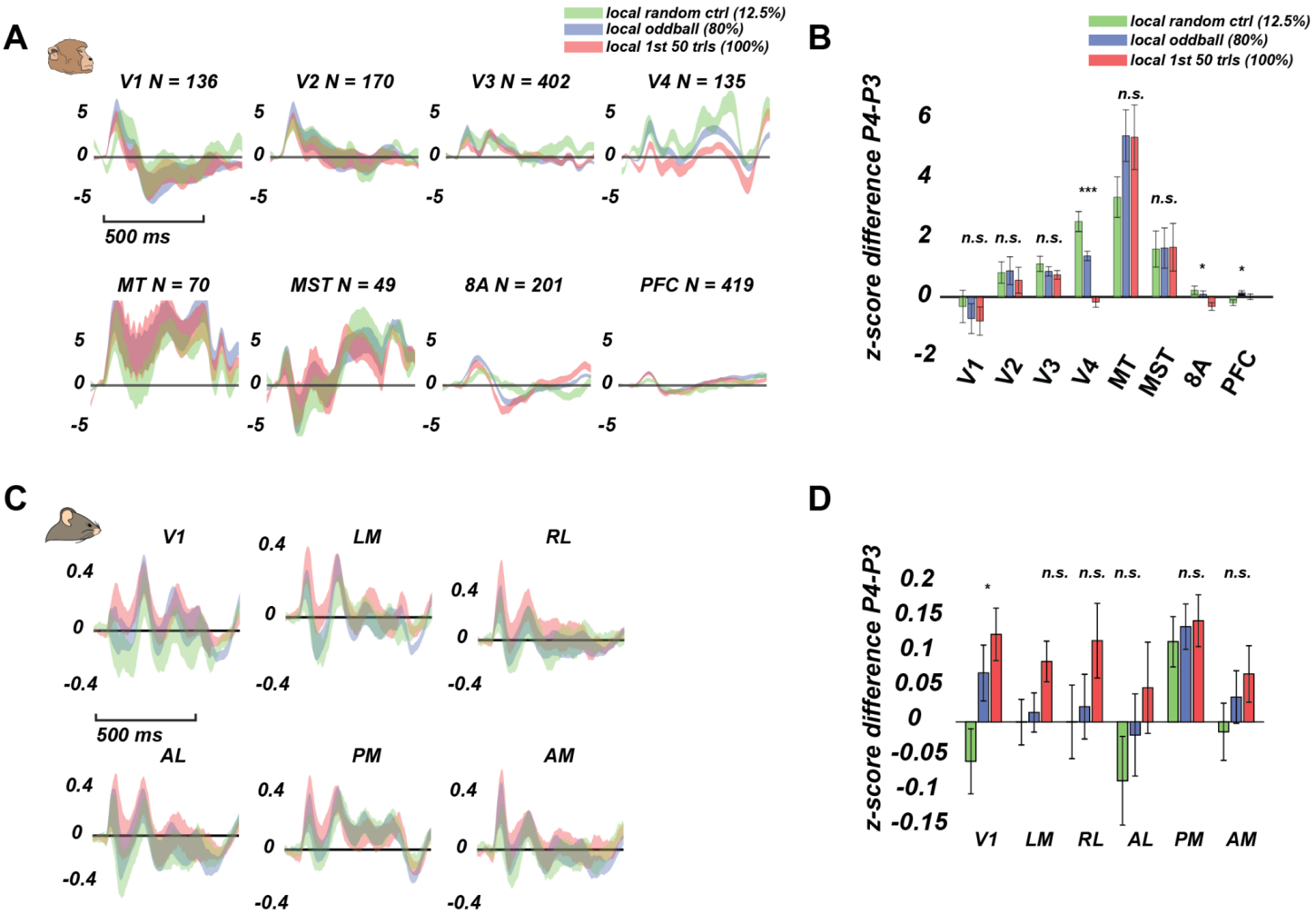

Fig. S9 Lack of prediction effect in local oddball sequence of various probabilities. (A, C) z-scored multiunit activity in monkeys and mice in response to local random control (12.5%, green), local oddball (80%, blue), and first 50 trials of local oddball (100%, red) across cortical hierarchy. Shadings show 2xSEM across units/channels. (B, D) z-score difference between P4 and P3 (effectively representing effect size) of local random control, local oddball, and first 50 trials of local oddball in monkeys and mice. Single asterisk represent $p<0.05$ from a one-way ANOVA test. Triple asterisk represent $p<0.001$ from a one way ANOVA test.

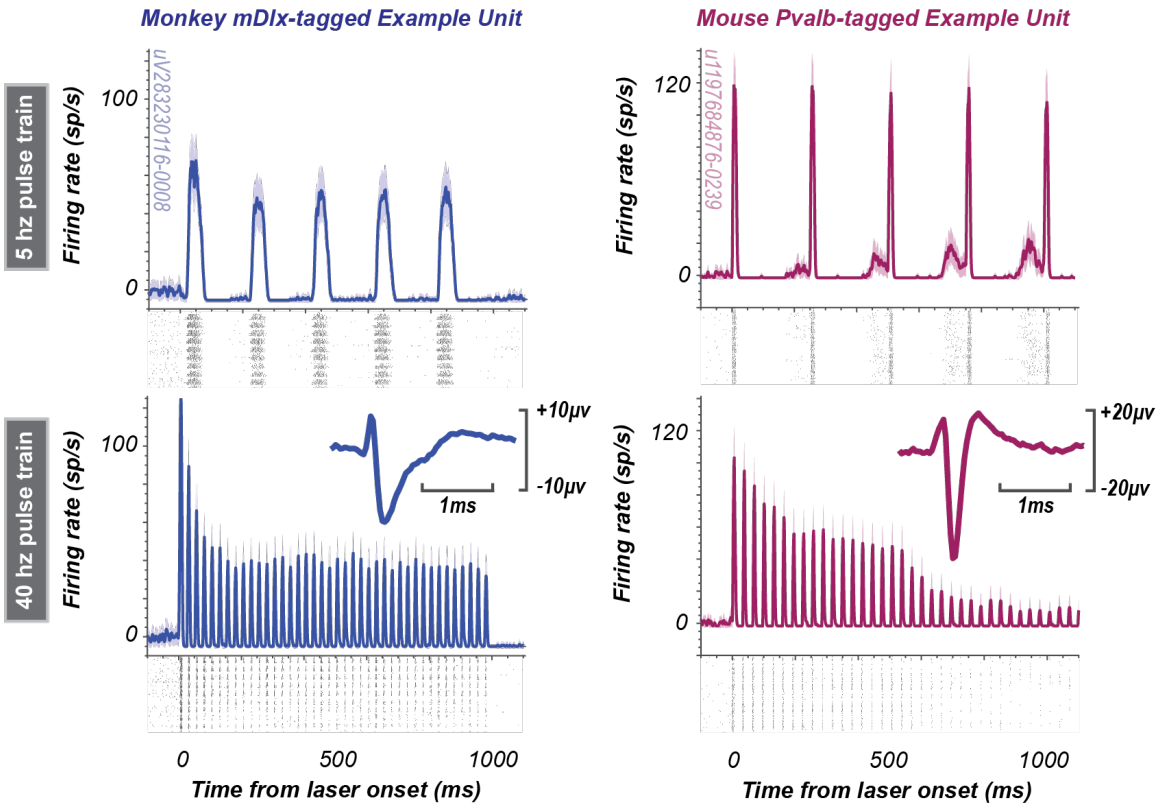

Fig. S10 Optogenetic identification of single units. Example units with optogenetics modulation to 5Hz (upper panels) and 40 Hz (lower panels) in monkeys (left panels, targeting pan-inhibitory interneurons) and in mice (right panels, in this example, targeting a Parvalbumin positive inhibitory interneuron). Traces indicate average smoothed firing rates (spikes per second) across trials (+/- SEM across trials). Rasters indicate individual spikes, stacked across trials. Insets indicate the average waveform shape of the identified unit.

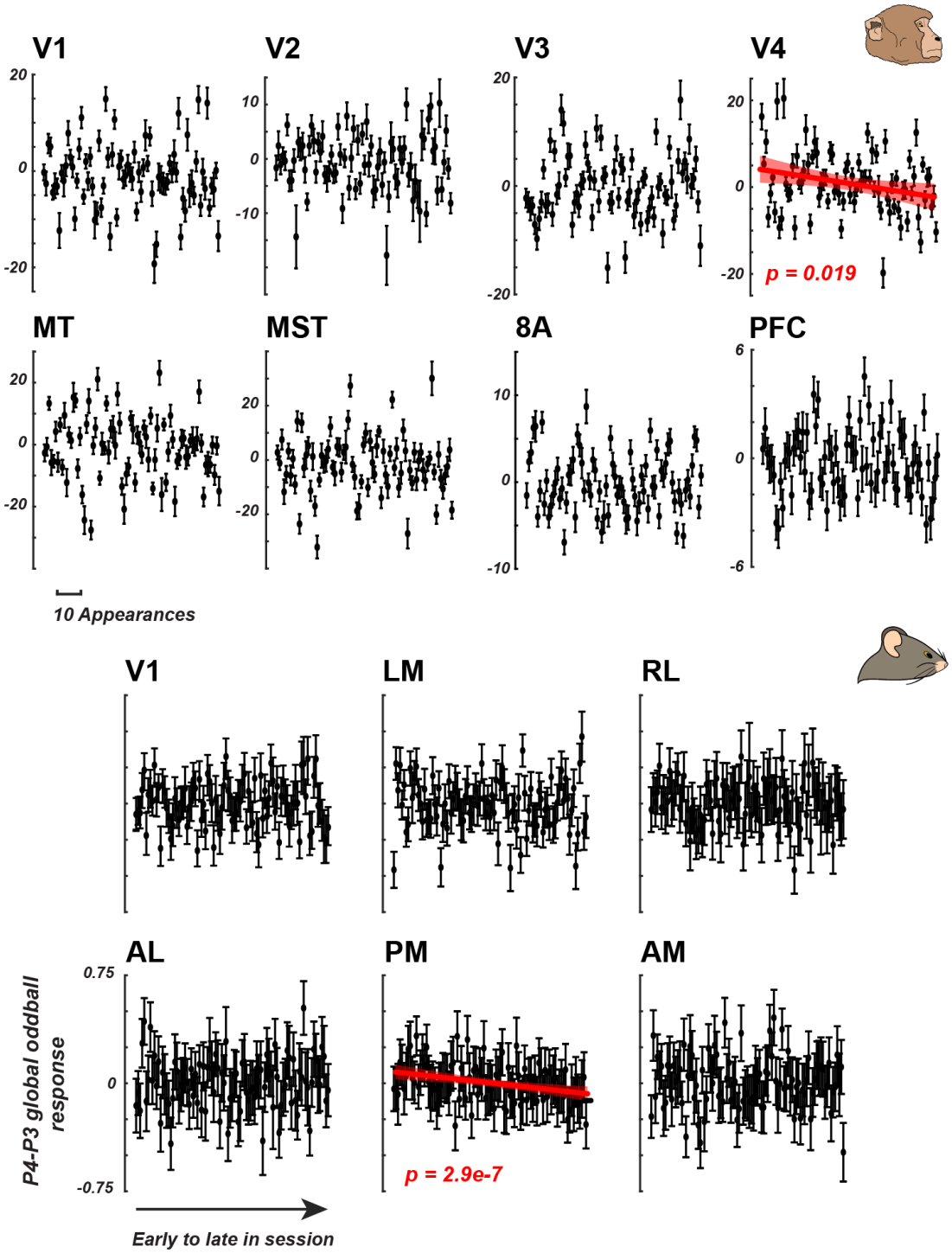

Fig. S11 Global oddball trials by position in the main block. Effect of global oddballs were examined by progression in main block. The order of occurrence of global oddball trials are plotted on the x axis. The neural responses of P4-P3 is plotted on the y-axis (mean across channels +/- 2SEM). Linear regressions between these variables were tested separately for each indicated area, and found to be significant in areas V4 in monkeys and PM in mice (P value indicated in graph). Only significant regression fits are plotted.